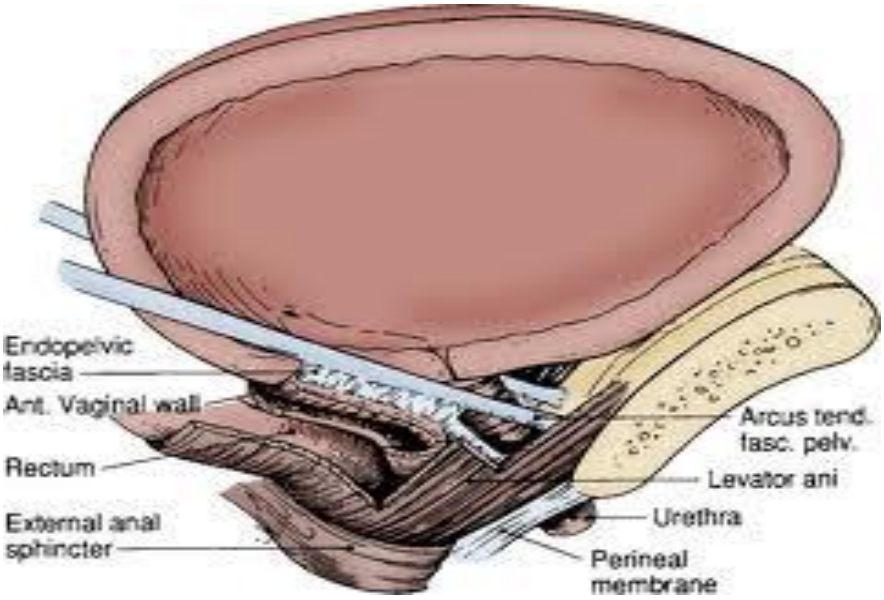

Fig 1.1.1.1. The role of the endopelvic fascia, arcus tendinius and levator ani in support of the urethra and bladder. Image obtained with permission from Wein: Campbell-Walsh Urology, 9th ed. Chapter 60, Elsevier.

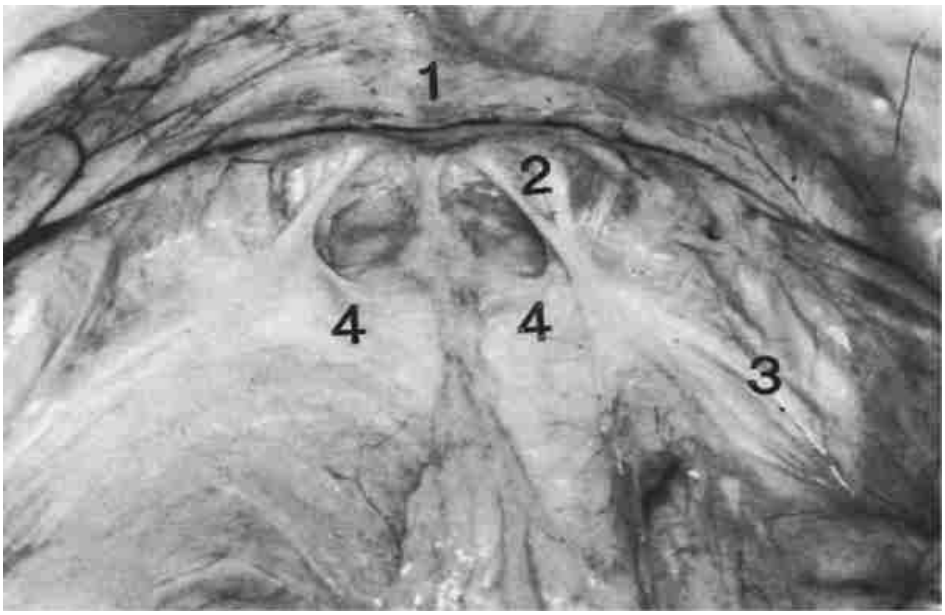

Fig 1.1.1.2. Inferior view of elderly female cadaver showing: 1) pubic bone, 2) right pubourethral ligament, 3) lateral endopelvic fascia forming the arcus tendinius fascia 4) central endopelvic fascia. Image obtained with permission f*rom Mostwin JL: Current concepts of female pelvic anatomy and physiology. Urol Clin North Am 1991;18:175-195.*

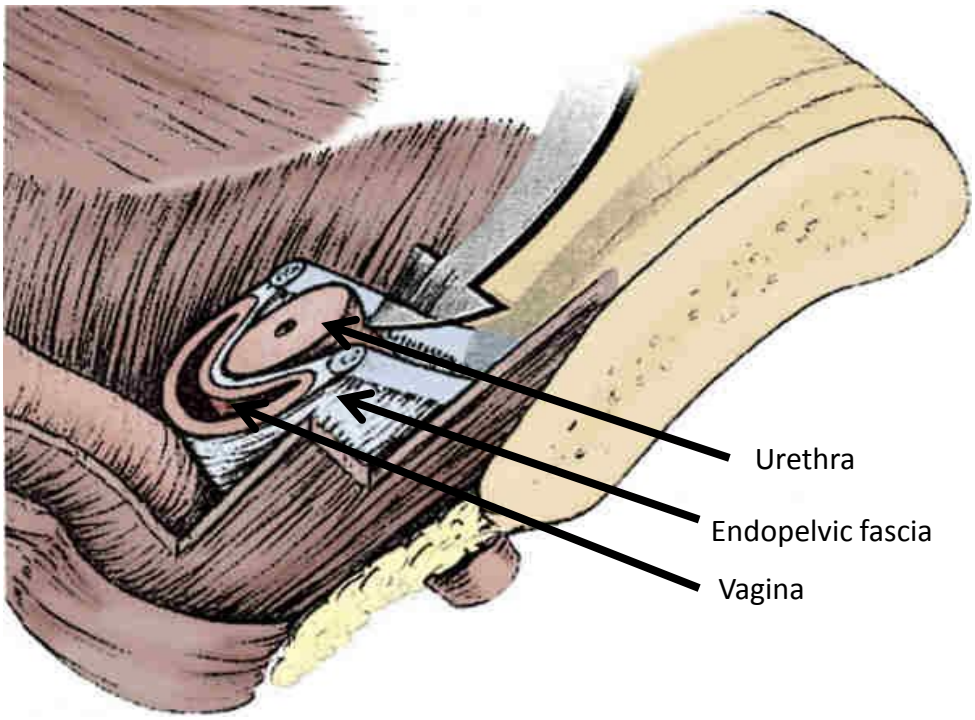

Fig 1.1.1.3. A view of the hammock theory by Ulmsten, the supporting structures to the urethra provide a backboard upon which the urethral contraction may be stabilised. Image obtained with permission from Wein: Campbell-Walsh Urology, 9th ed. Chapter 60, Elsevier.

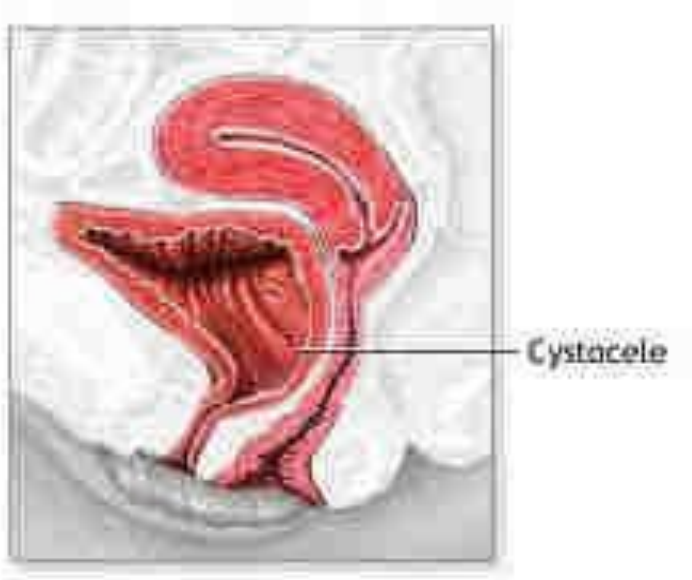

Fig 1.2.1. Anterior compartment prolapse due to a cystocele. Image obtained with permission from MD consult, Elsevier.

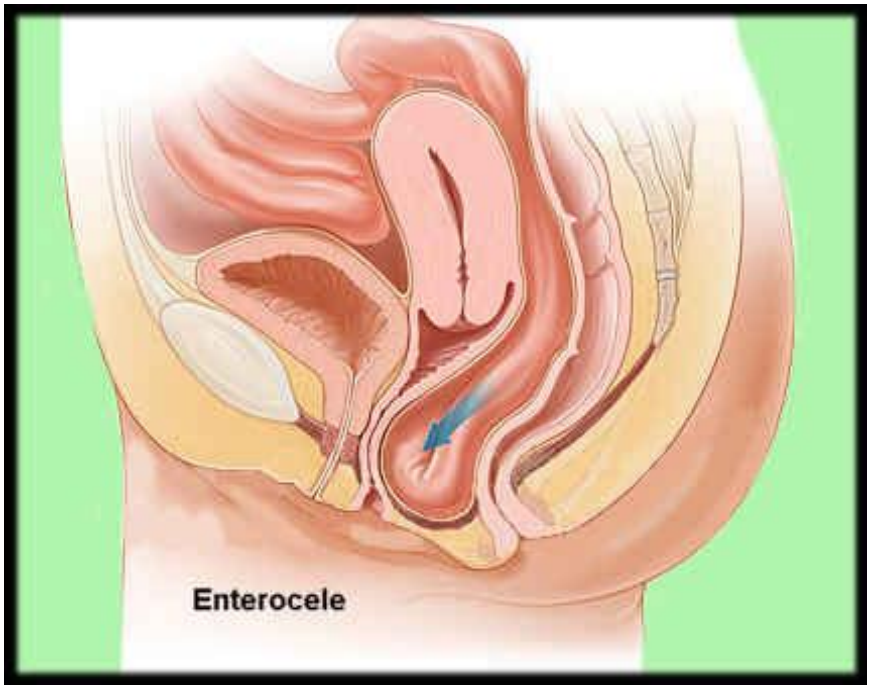

Fig 1.2.2. Middle compartment prolapse due to an enterocele. Image obtained with permission from MoonDragon Birthing service, Salem Massachusetts.

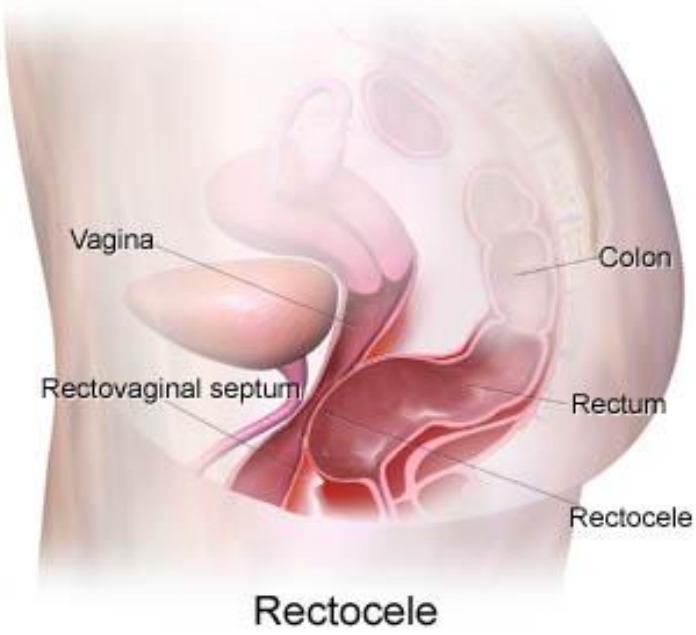

Fig 1.2.3. Posterior compartment prolapse due to a rectocele. Image obtained with permission from Allina hospitals and clinics.

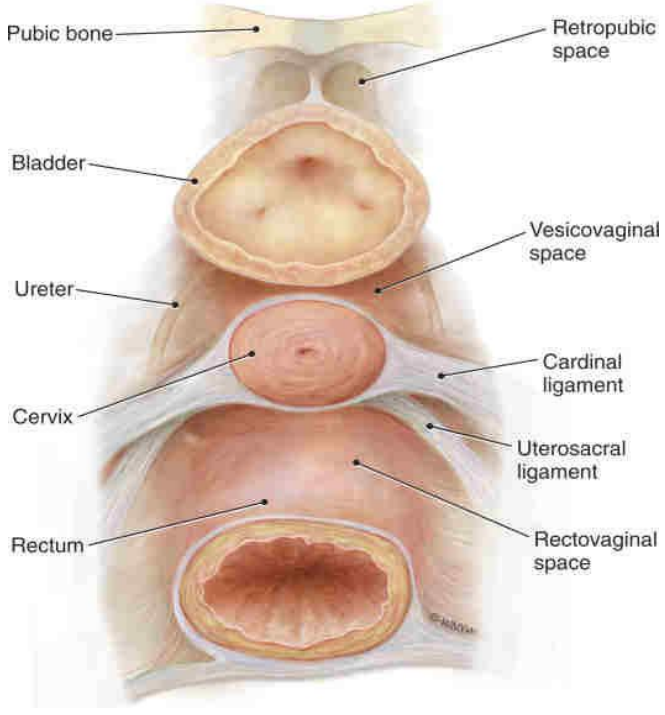

Fig 1.2.1.1. Coronal view of the level 1 supports of the urethra. Image obtained with permission from Wein: Campbell-Walsh Urology, 9th ed. Chapter 60, Elsevier.

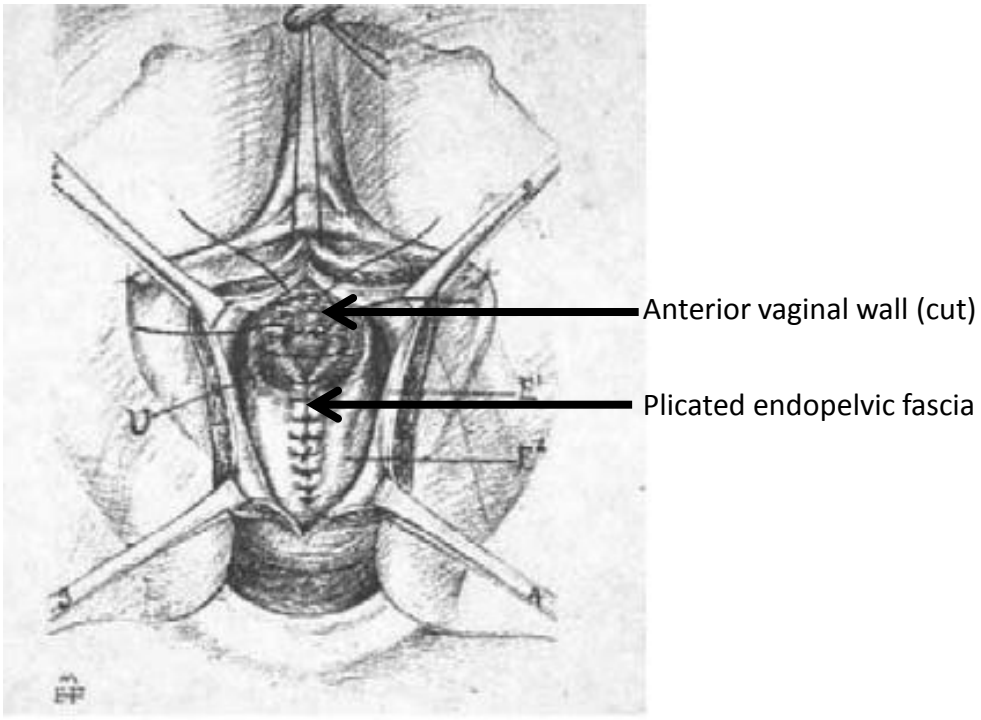

Fig 1.3.2.1. Anterior vaginal repair illustrating sutures plicating endopelvic fascia in the midline. Image obtained with permission from Pathophysiology of Urinary incontinence, Health publications Ltd, Paris.

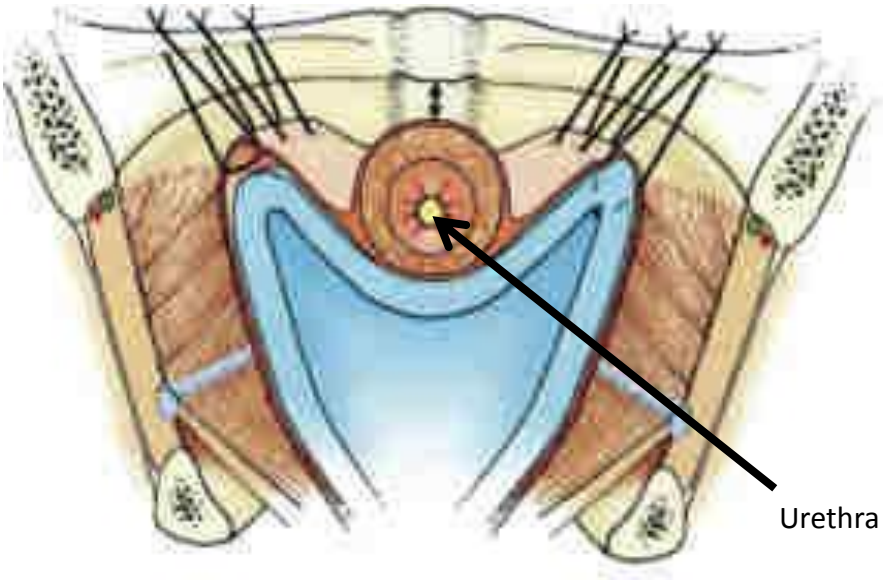

Fig 1.3.2.2. Colposuspension- illustrating sutures elevating the para-urethral fascia towards Cooper's ligament. Image obtained with permission from Wein: Campbell-Walsh Urology, 9th ed. Chapter 60, Elsevier.

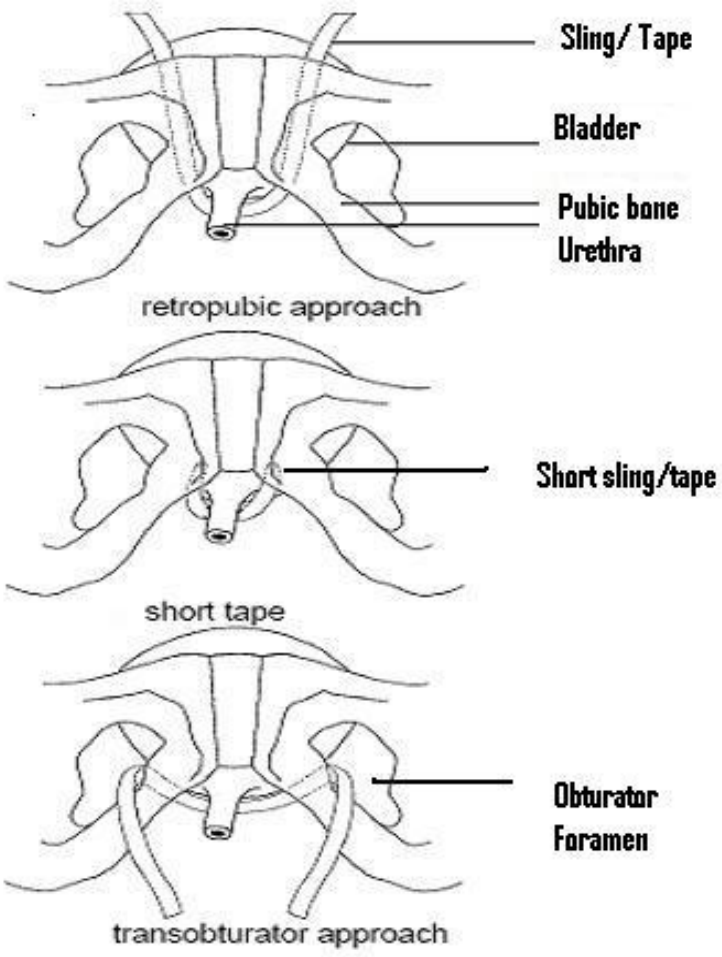

Fig 1.3.2.3. Variations of the sling/tape procedure.

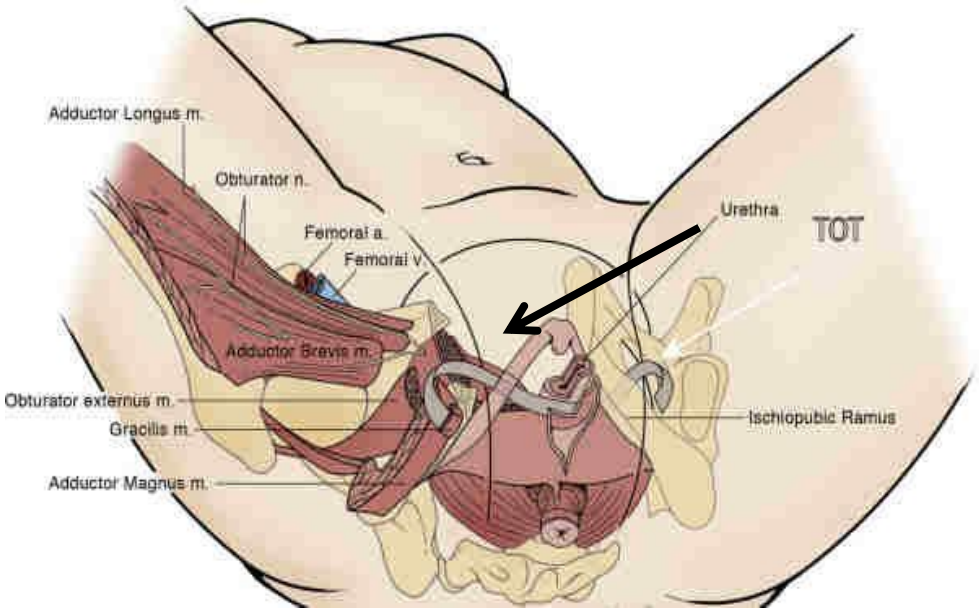

Fig 1.3.2.4. TOT procedure showing the regional anatomy. Image obtained with permission from Wein: Campbell-Walsh Urology, 9th ed. Chapter 60, Elsevier.

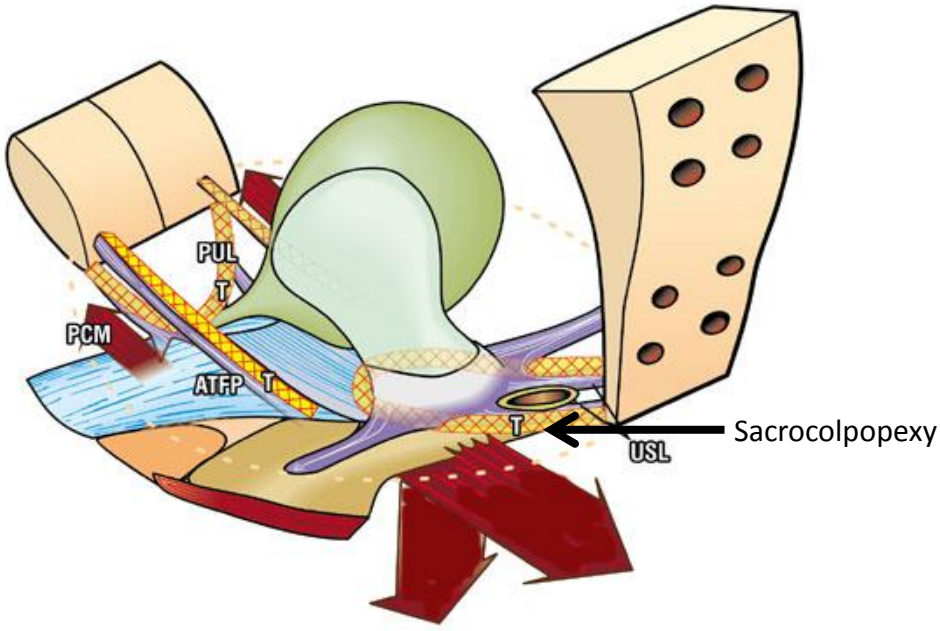

Figure 1.4.2.1.1. Showing the common positions of tapes (T) for the treatment of SUI/POP. ATFP- Arcus Tendinius Fascia Pelvis, PCM-Pubococcygeus muscle, PUL-Pubourethral ligament and USL-Uterosacral ligament. Image obtained with permission from http://www.integraltheory.org/anatomy/index.html.

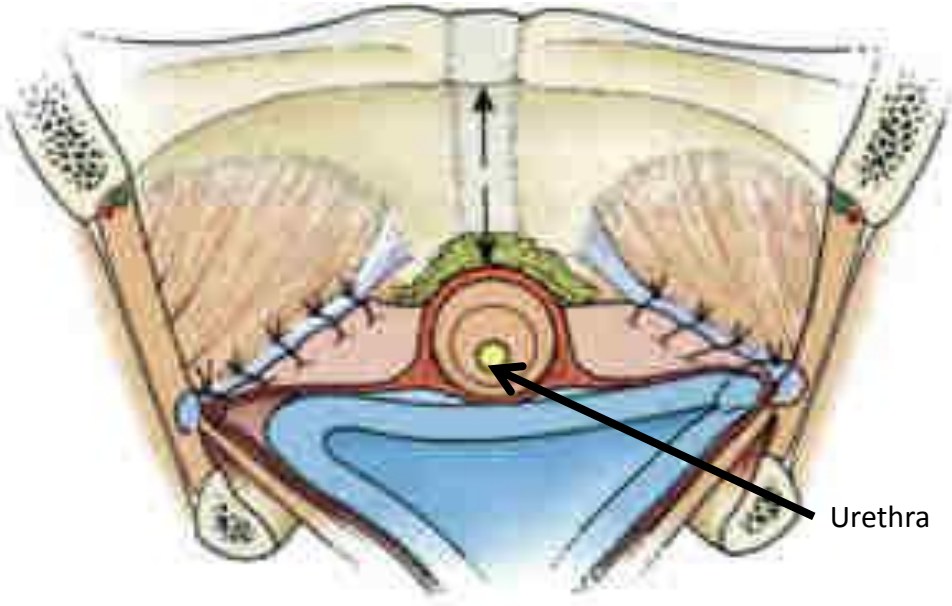

Fig 1.4.2.2.1. Paravaginal repair. Image obtained with permission from Wein: Campbell-Walsh Urology, 9th ed. Chapter 60, Elsevier.

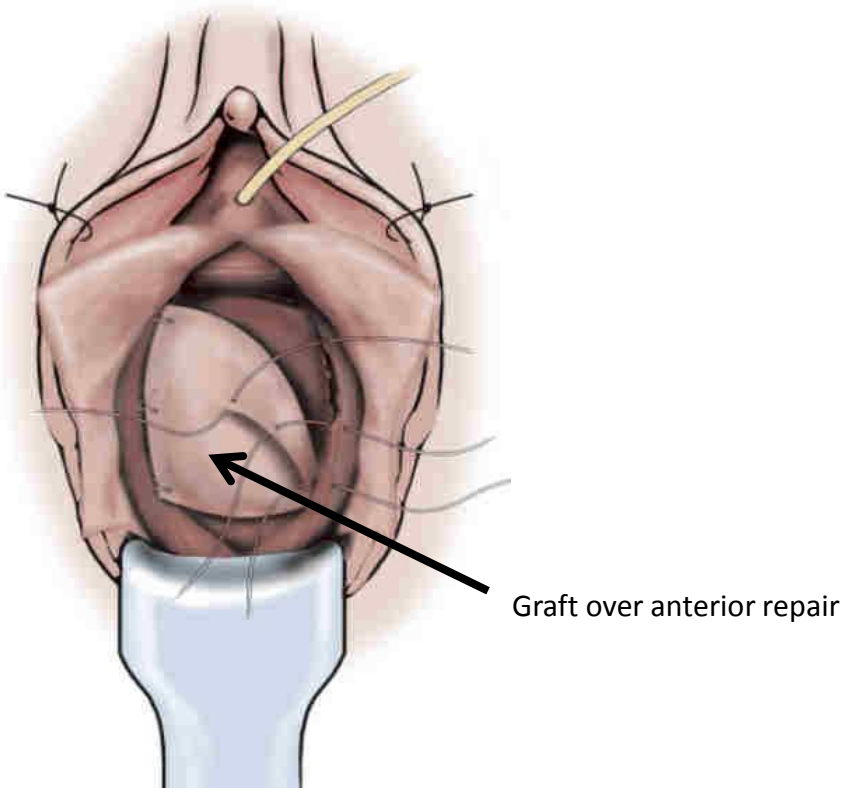

Fig 1.4.2.2.2. Anterior repair followed by application of a graft shown on to the arcus tendinuis fascia pelvis. Image obtained with permission from Wein: Campbell-Walsh Urology, 9th ed. Chapter 60, Elsevier.

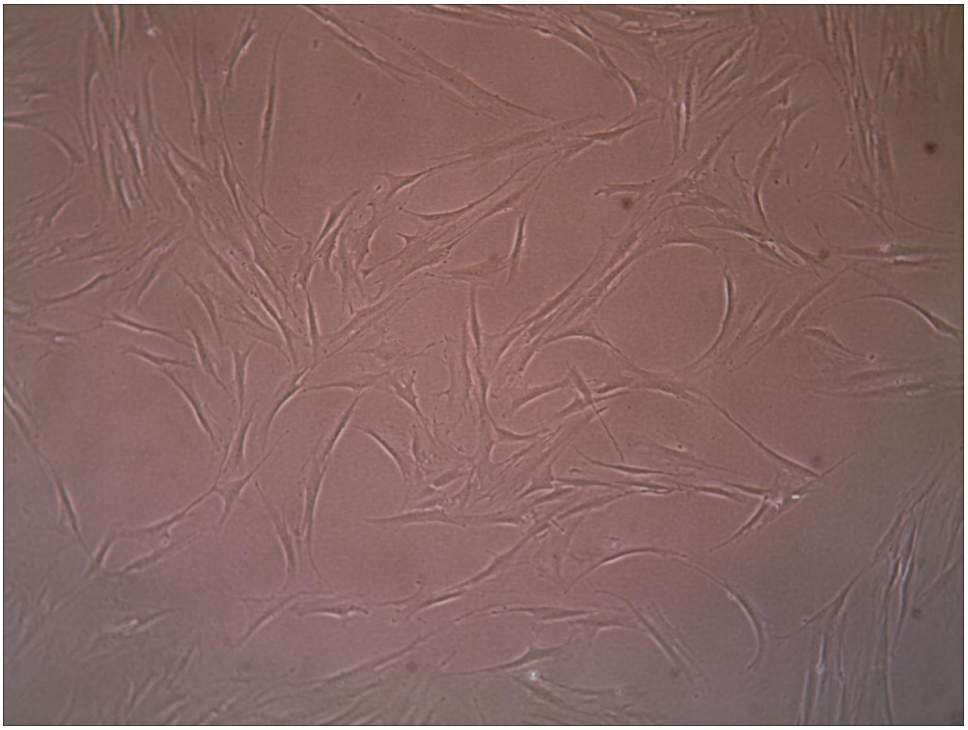

Fig 1.8.2.1. Image of fibroblasts from a microscope (X100 magnification).

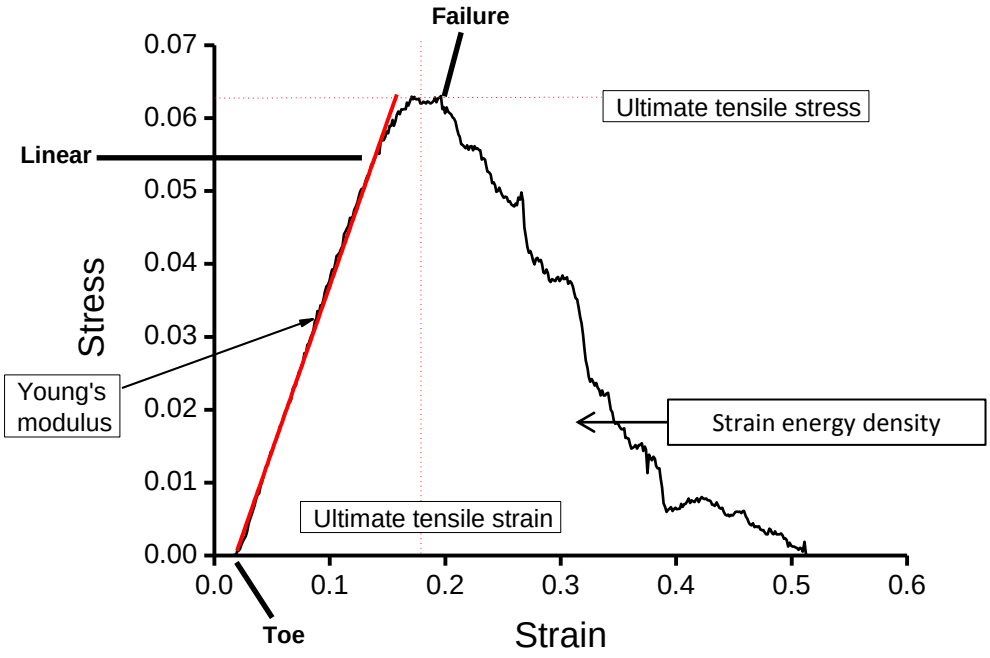

Fig 1.10.1. The plot of Strain Vs Stress. The ultimate tensile strength is the maximum stress at break point, Ultimate strain is the strain at the ultimate tensile strength and the Young's modulus is the gradient of the linear portion of the curve.

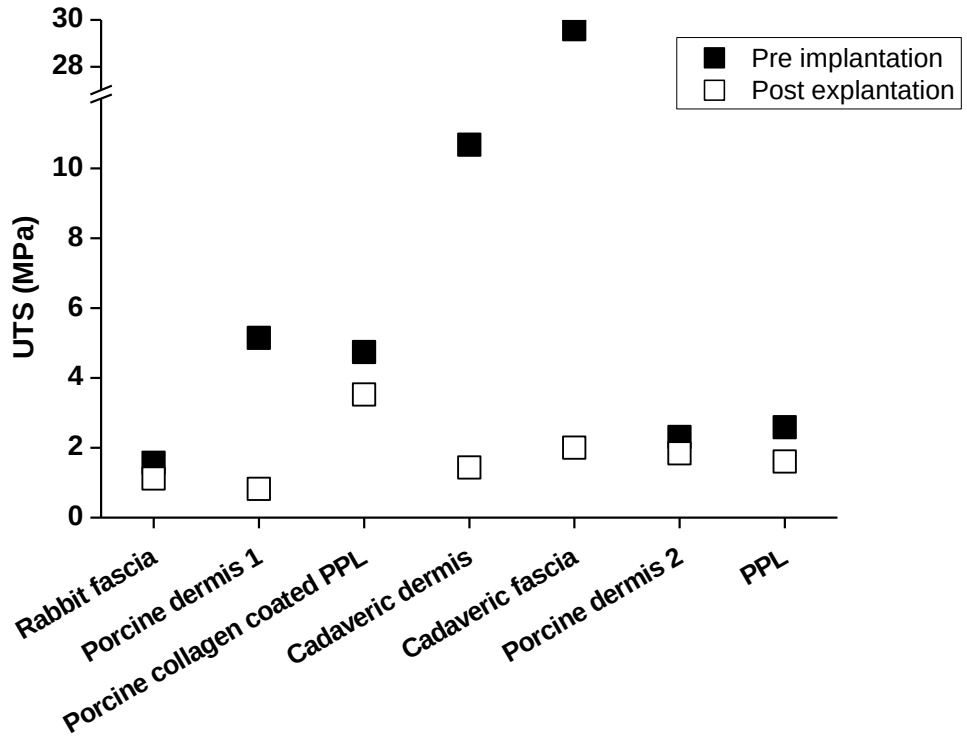

Fig 1.10.4.1. The change in ultimate tensile strength of pelvic organ prosthesis post explantation from rabbit paravaginal tissue.

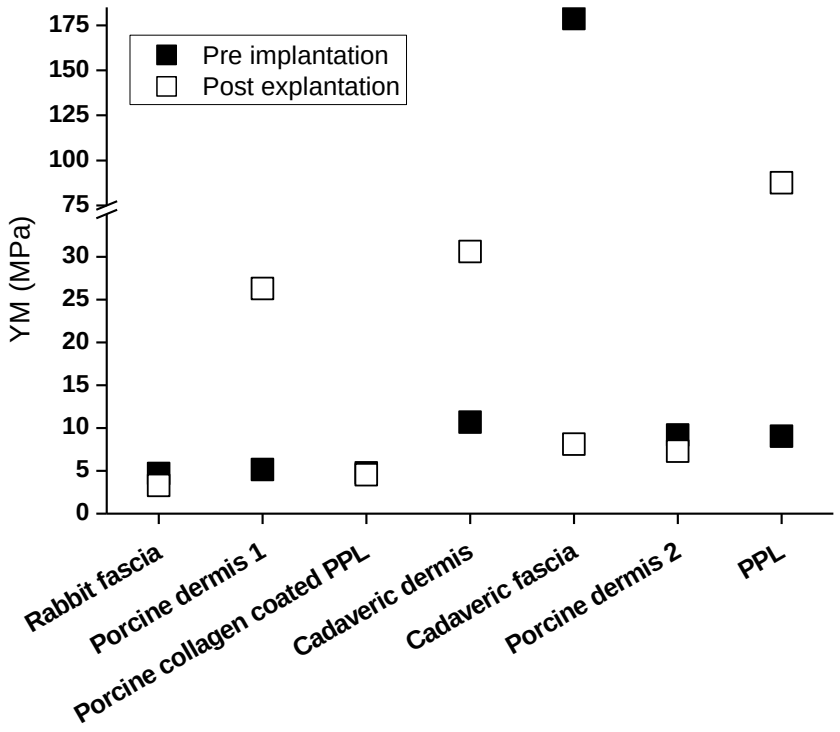

Fig 1.10.4.2. The change in Young's modulus of pelvic organ prosthesis post explantation from rabbit paravaginal tissue.

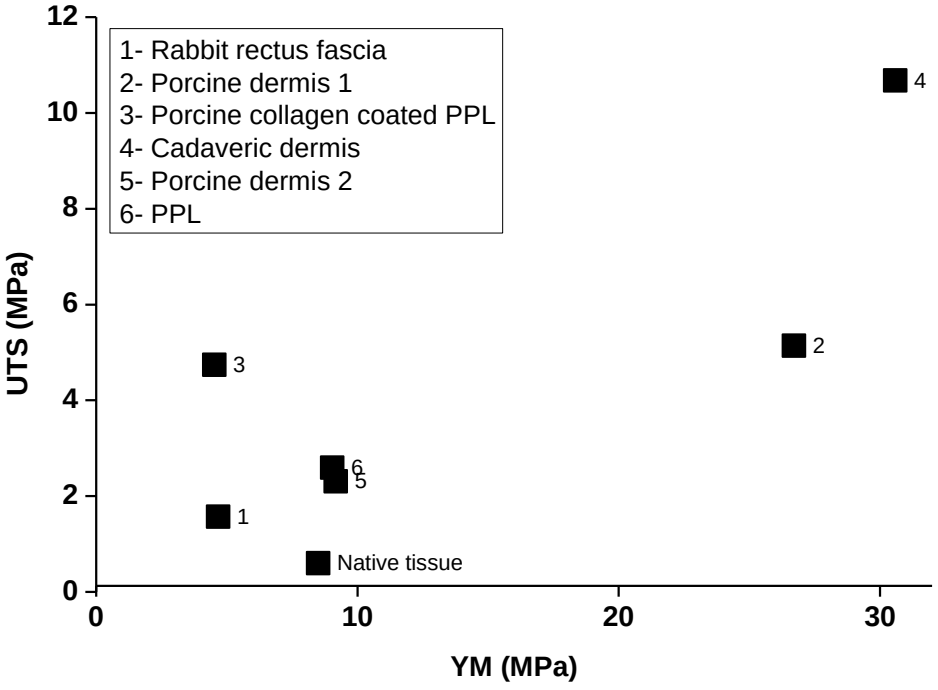

Fig 1.10.5.1. The Young's modulus and ultimate tensile strength of prostheses in relation to native tissue.

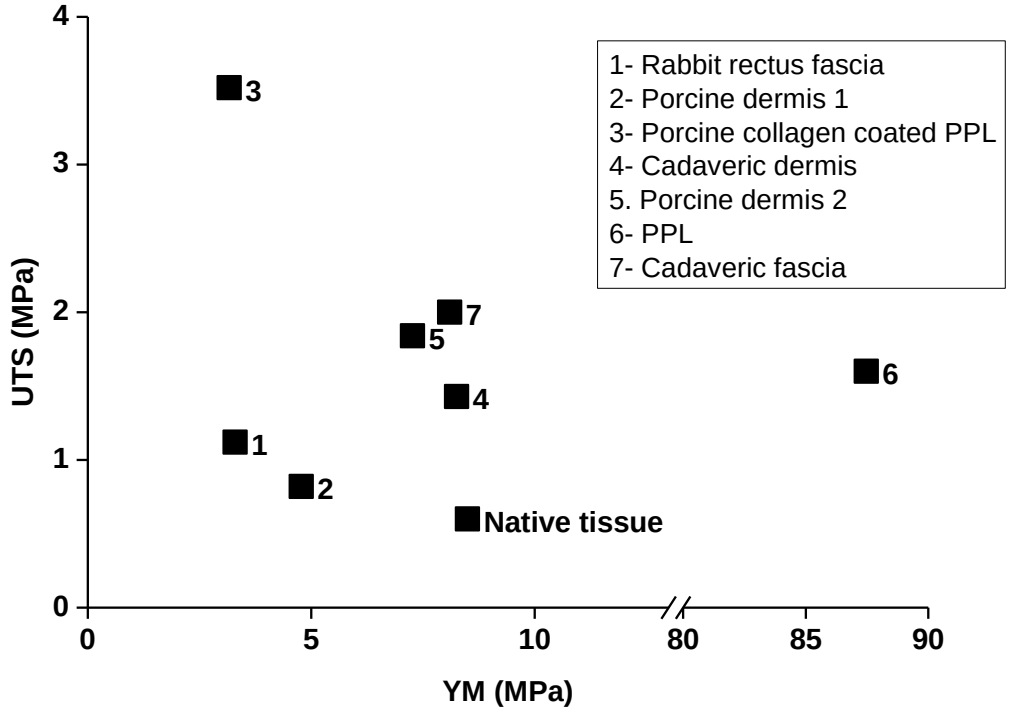

Fig 1.10.5.2. The Young's modulus and ultimate tensile strength of prostheses post explantation in relation to native tissue.

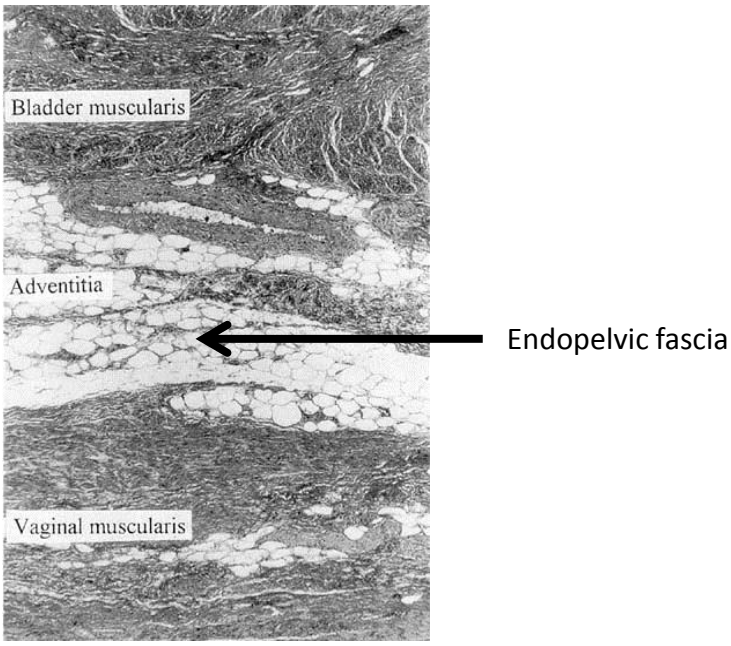

Fig 1.11.1. H&E of a full thickness section through the vagina and bladder wall with intervening endopelvic fascia (adventitia), magnification X40. Image obtained with permission from Weber AM, Walters MD. Anterior vaginal prolapse: review of anatomy and techniques of surgical repair. Obstet Gynecol 1997; 89:311-318.

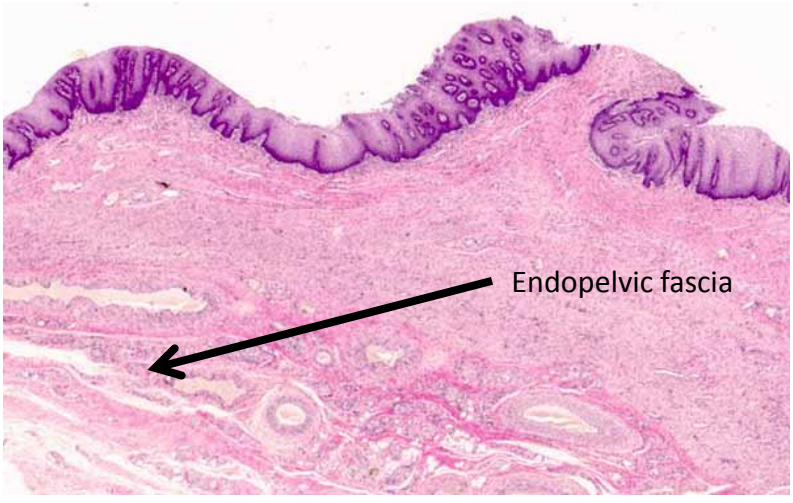

Fig 1.11.2. H&E staining of vaginal tissue (X40). The connective tissue in the bottom of the picture represents the endopelvic fascia. Obtained with permission from Farrell SA, Dempsey T, Geldenhuys L. Histologic examination of "fascia" used in colporrhaphy. Obstet Gynecol 2001; 98:794-798.

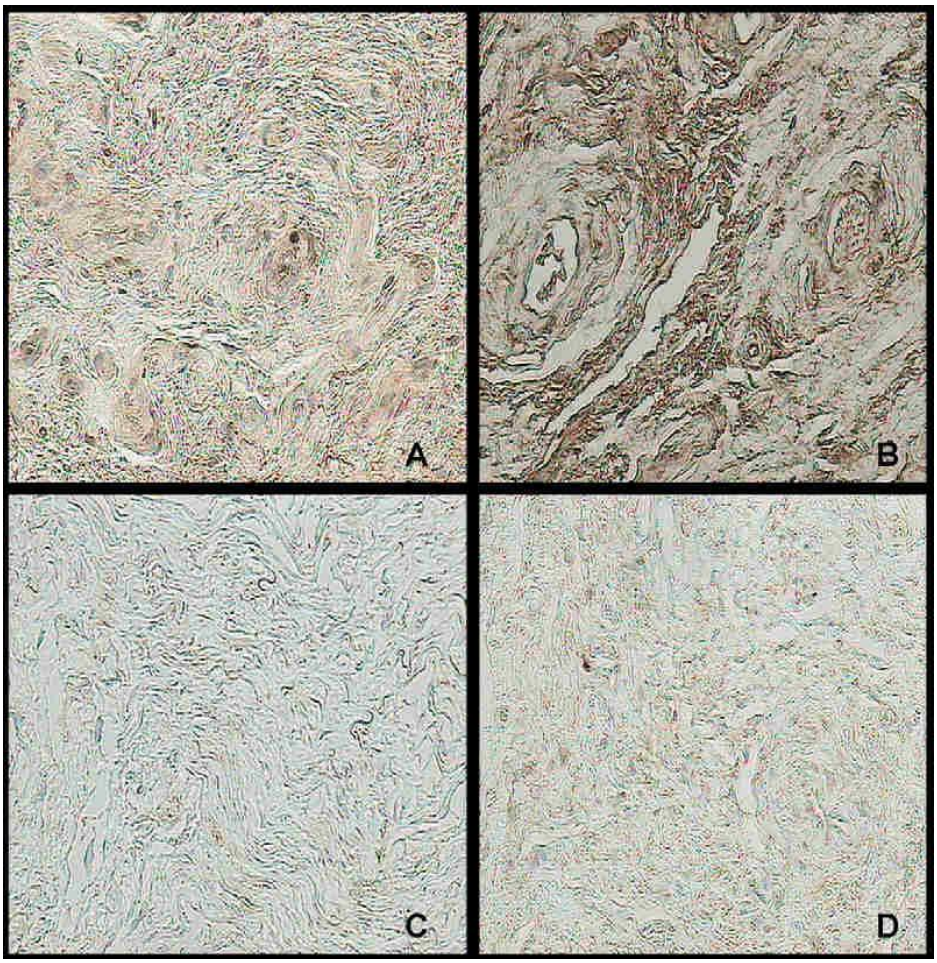

Fig 1.11.1.1. Microscopic appearance of paravaginal tissue, after immunohistochemical staining for collagen I,(mag X150) from a) Premenopausal women with SUI, b) Premenopausal women without SUI, c) Postmenopausal women with SUI, d) Postmenopausal women without SUI. Image obtained with permission form Trabucco E, Soderberg M, Cobellis L, *et al*. N. Role of proteoglycans in the organization of periurethral connective tissue in women with stress urinary incontinence. Maturitas 2007; 58:395-405.

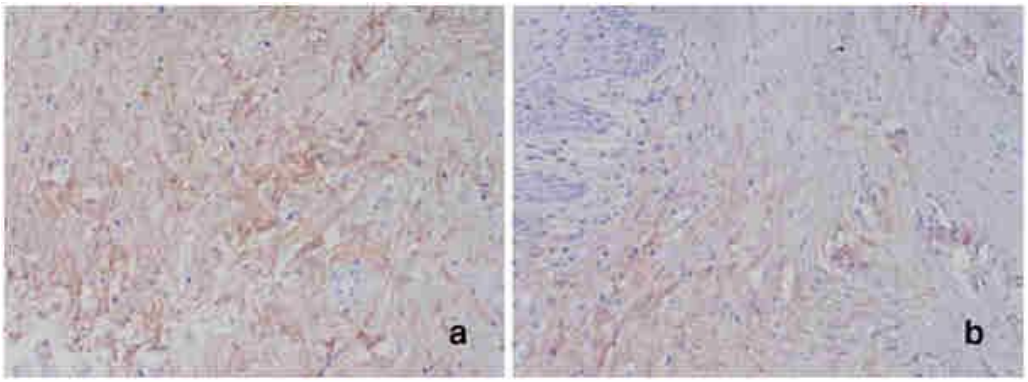

Fig 1.11.1.2. Microscopic appearance of paravaginal tissue, after immunohistochemical staining for collagen III, (mag X200) from a) women with SUI, b) women without SUI. Image obtained with permission from; Song Y, Hong X, Yu Y, Lin Y. Changes of collagen type III and decorin in paraurethral connective tissue from women with stress urinary incontinence and prolapse. Int Urogynecol J Pelvic Floor Dysfunct 2007; 18:1459-1463.Springer.

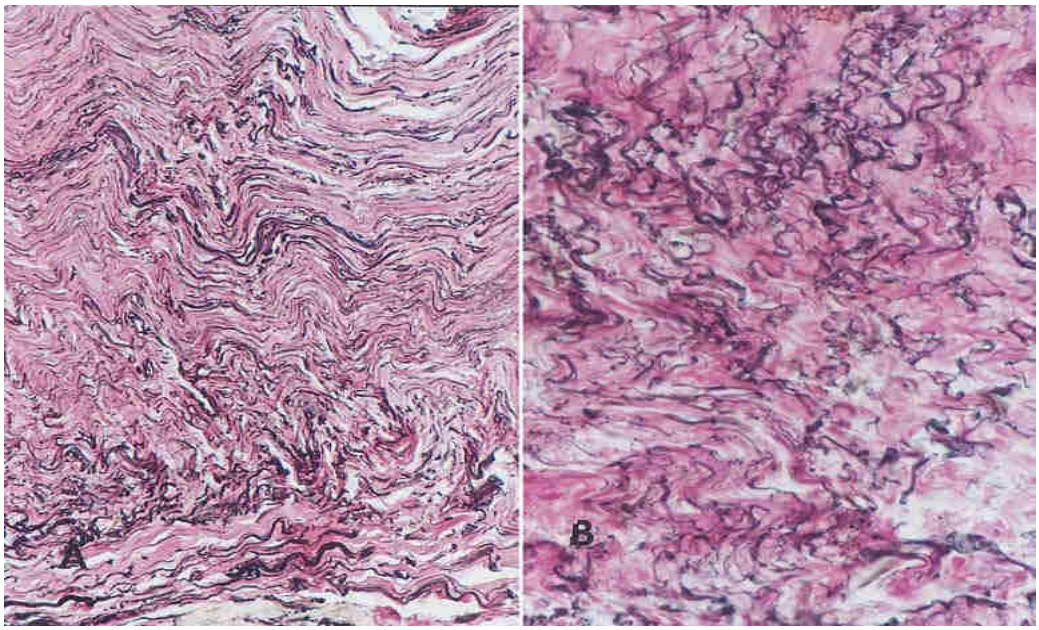

Fig 1.11.2.1. Elastic fibres in endopelvic fascia of women with SUI as viewed after staining with van Geison stain, a) Mag x160, b) Mag x240. Image obtained with permission from Cor A, Barbic M, Kralj B. Differences in the quantity of elastic fibres and collagen type I and type III in endopelvic fascia between women with stress urinary incontinence and controls. Urol Res 2003; 31:61-65, Springer.

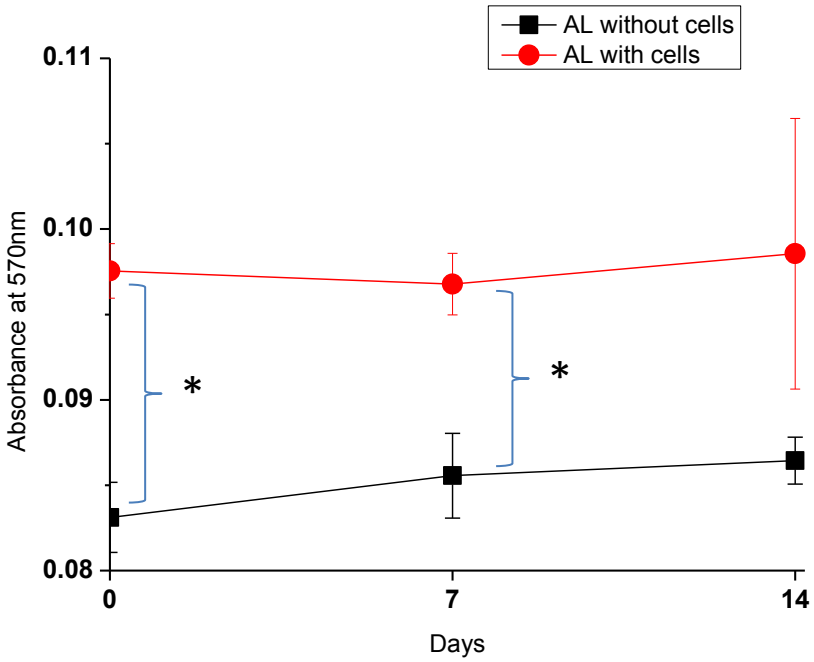

Fig 3.2.1.1. The metabolic activity of fibroblasts on Alloderm, as assessed by absorbance of AlamarBlue stain at 570nm, (n=9±SEM), *p<0.05.

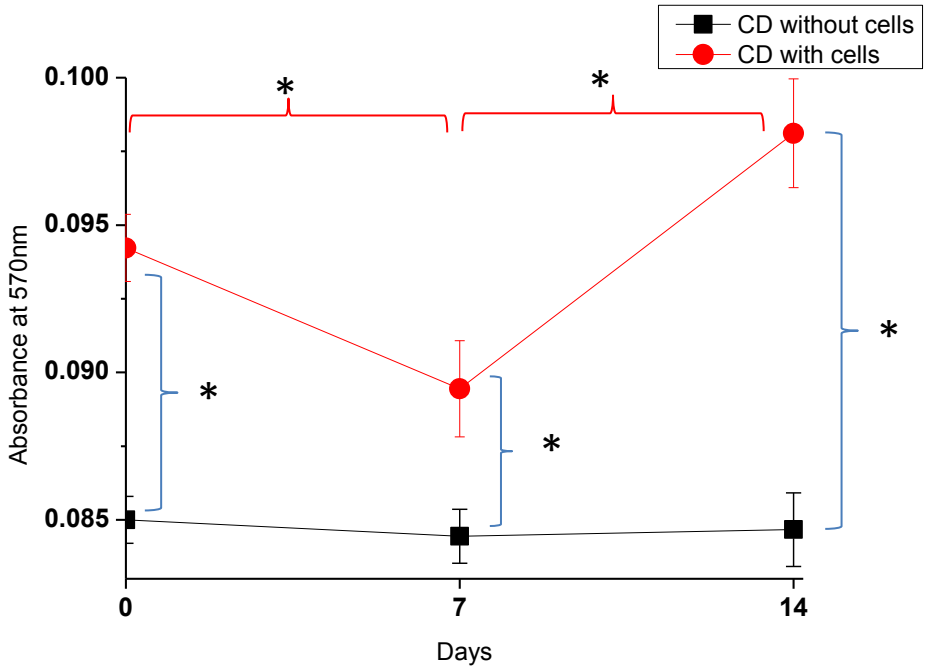

Fig 3.2.2.1. The metabolic activity of fibroblasts on Cadaveric dermis, as assessed by absorbance of AlamarBlue stain at 570nm, (n=9±SEM), *p<0.05.

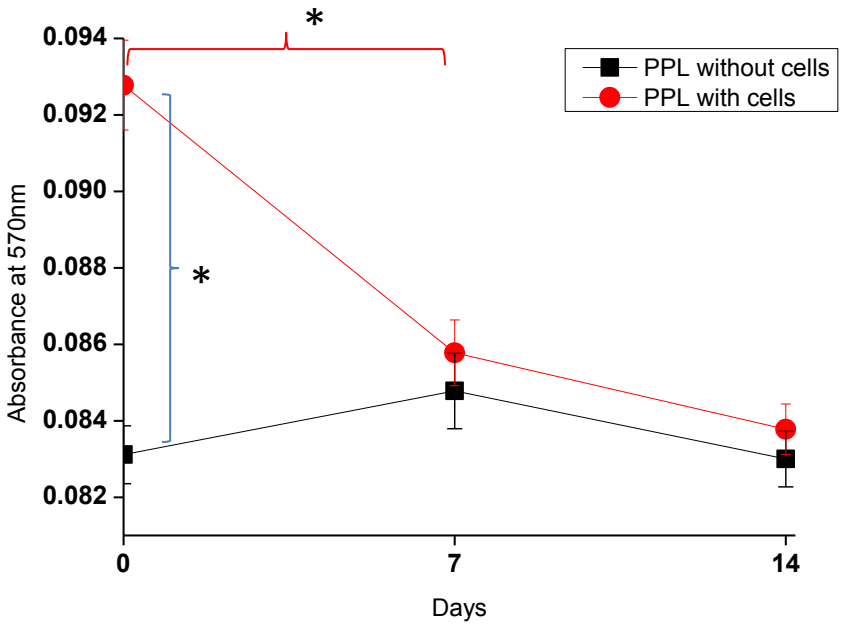

Fig 3.2.3.1. The metabolic activity of fibroblasts on polypropylene, as assessed by absorbance of AlamarBlue stain at 570nm, (n=9±SEM), *p<0.05.

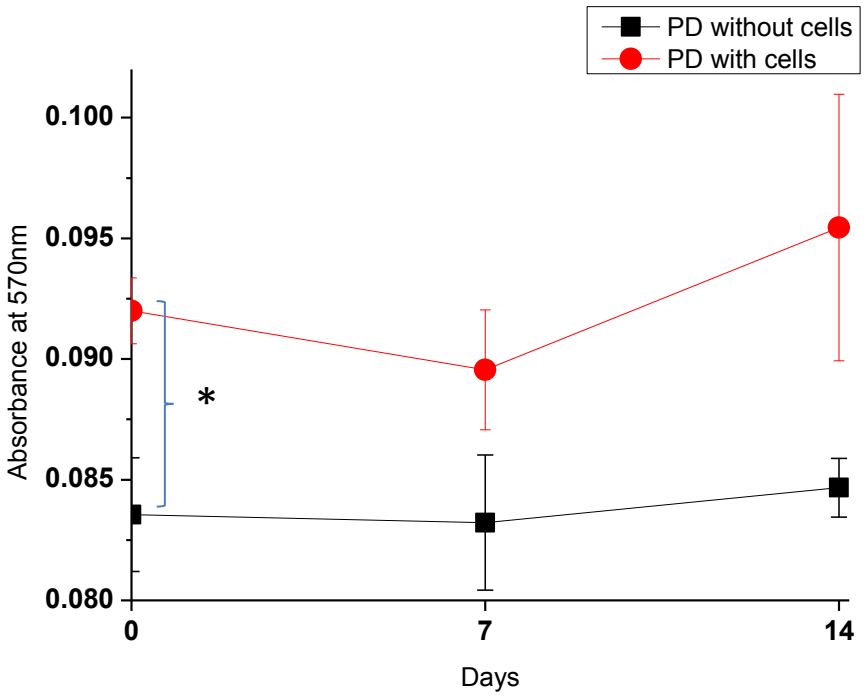

Fig 3.2.4.1. The metabolic activity of fibroblasts on porcine dermis, as assessed by absorbance of AlamarBlue stain at 570nm, (n=9±SEM), *p<0.05.

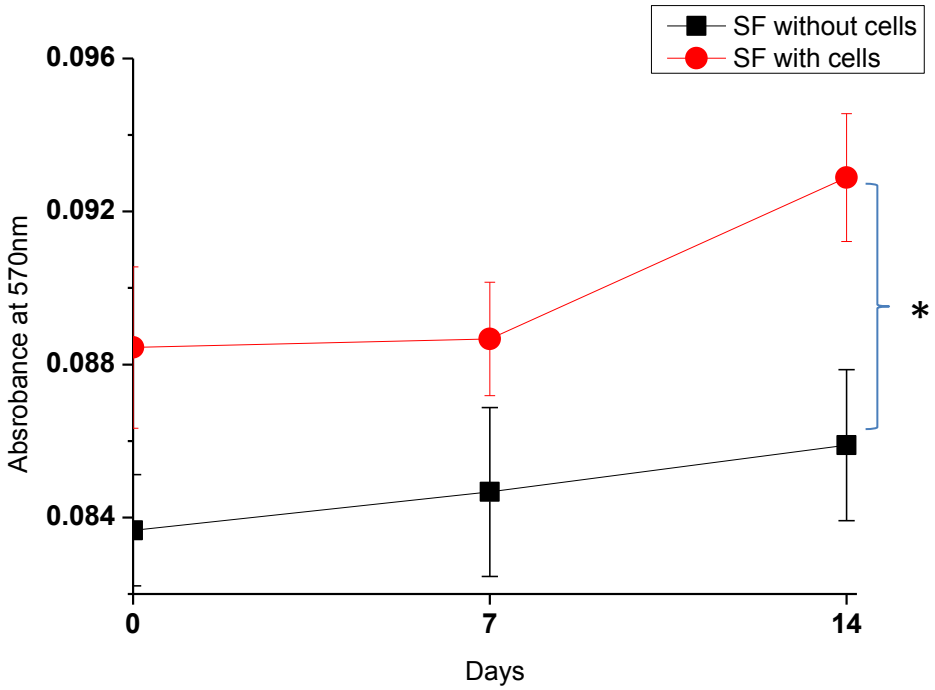

Fig 3.2.5.1. The metabolic activity of fibroblasts on sheep forestomach, as assessed by absorbance of AlamarBlue stain at 570nm, (n=9±SEM), *p<0.05.

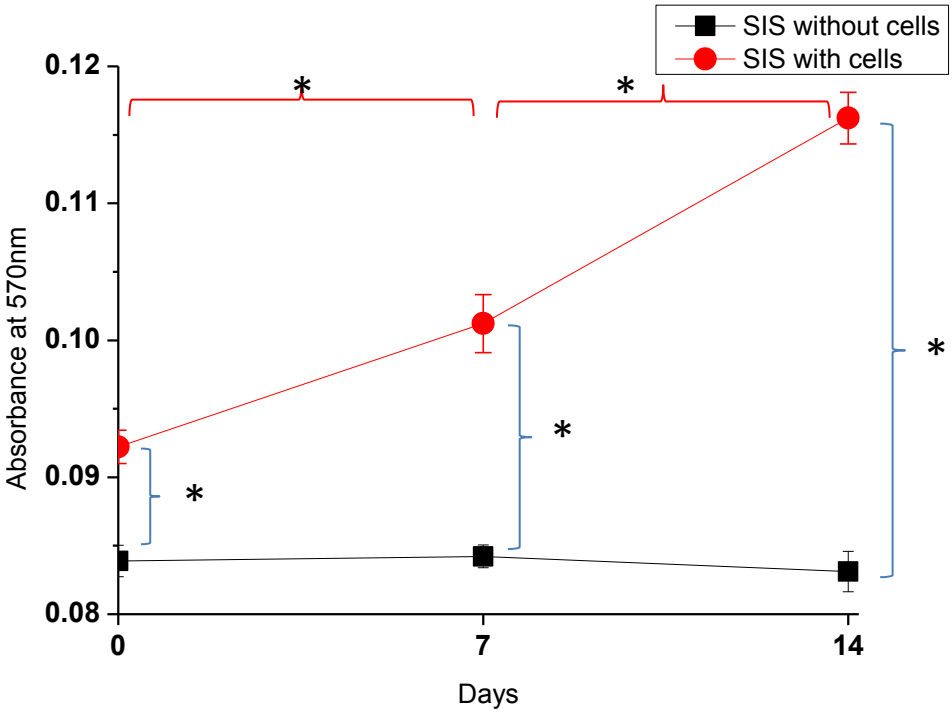

Fig 3.2.6.1. The metabolic activity of fibroblasts on small intestinal submucosa, as assessed by absorbance of AlamarBlue stain at 570nm, (n=9±SEM), *p<0.05.

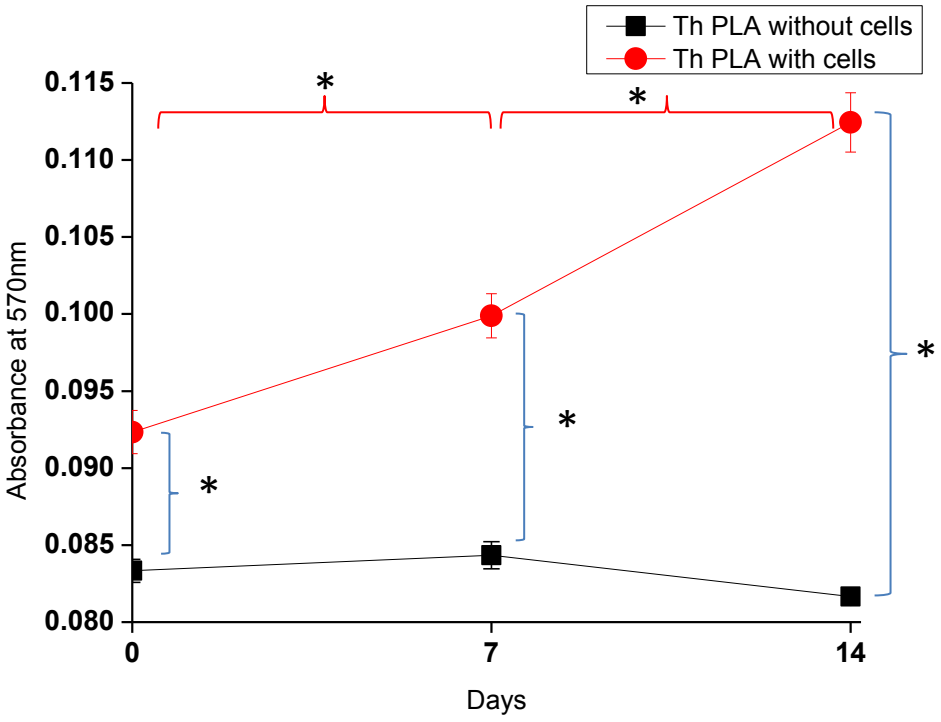

Fig 3.2.7.1. The metabolic activity of fibroblasts on Thermoannealed PLA, as assessed by absorbance of AlamarBlue stain at 570nm, (n=9±SEM), *p<0.05.

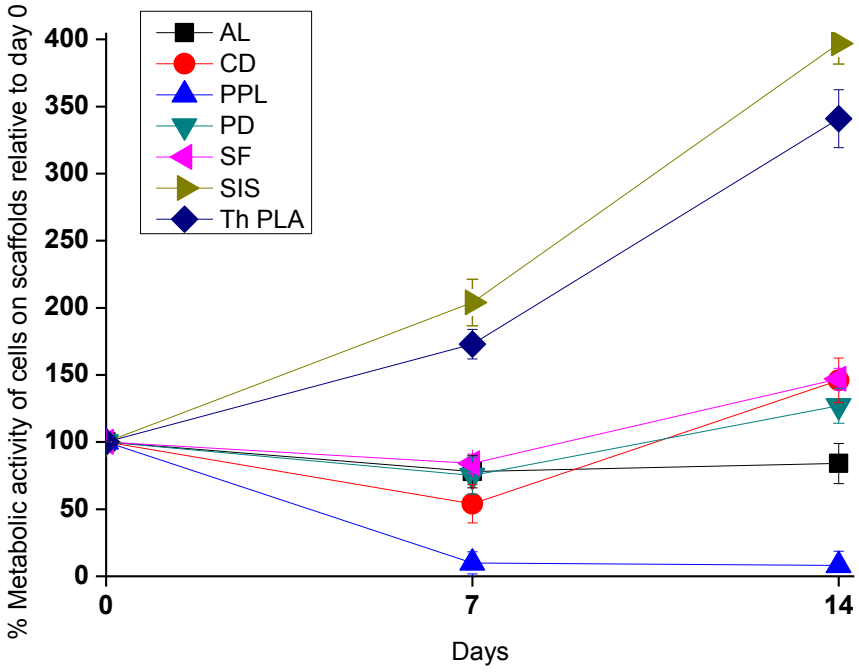

Fig 3.3.1. The metabolic activity of fibroblasts on the seven scaffolds over 14 days, as assessed by absorbance of AlamarBlue stain at 570nm, (n=9±SEM).

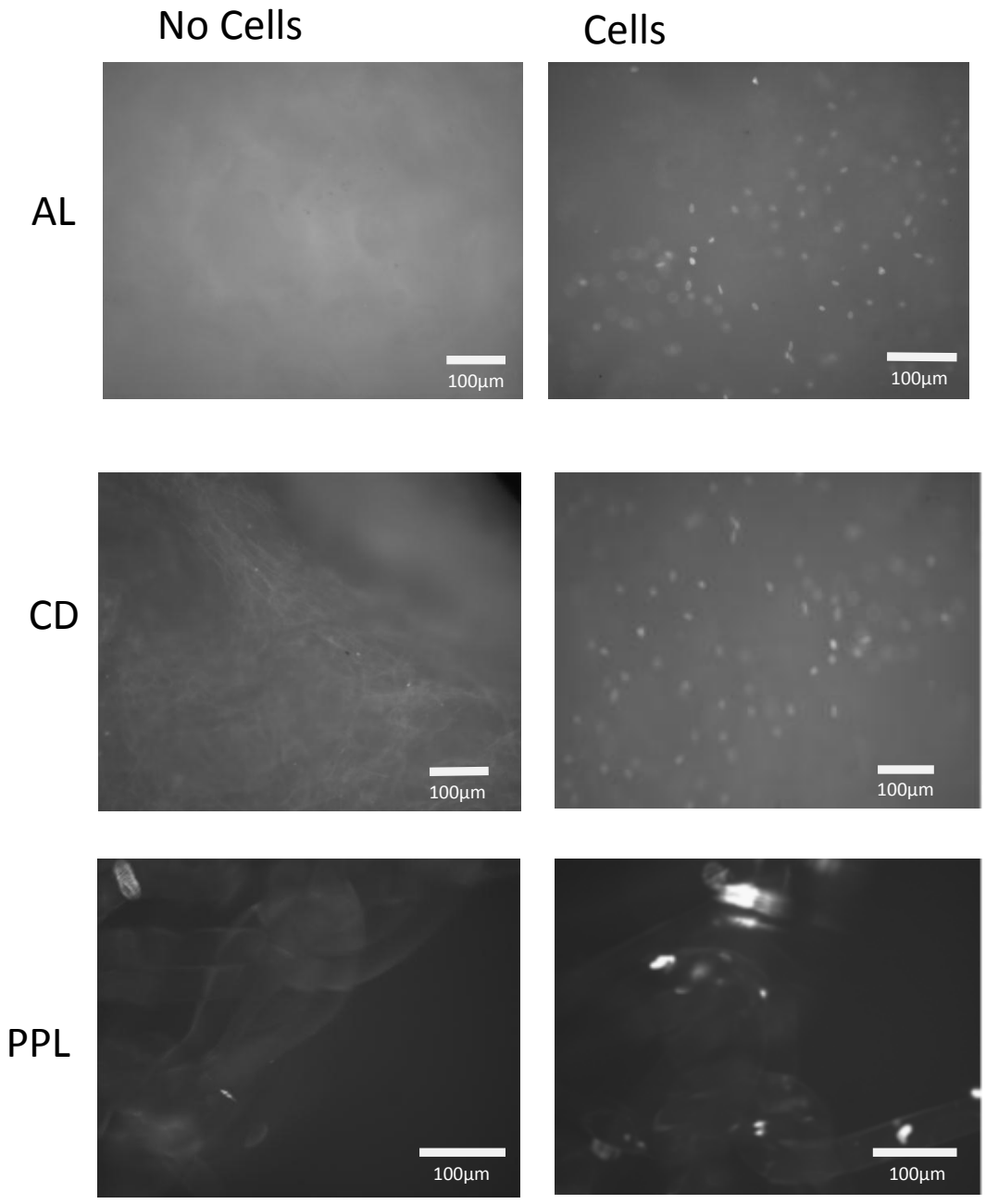

Fig 3.4.1. The distribution of fibroblasts on the seven scaffolds as seen on DAPI stained images.

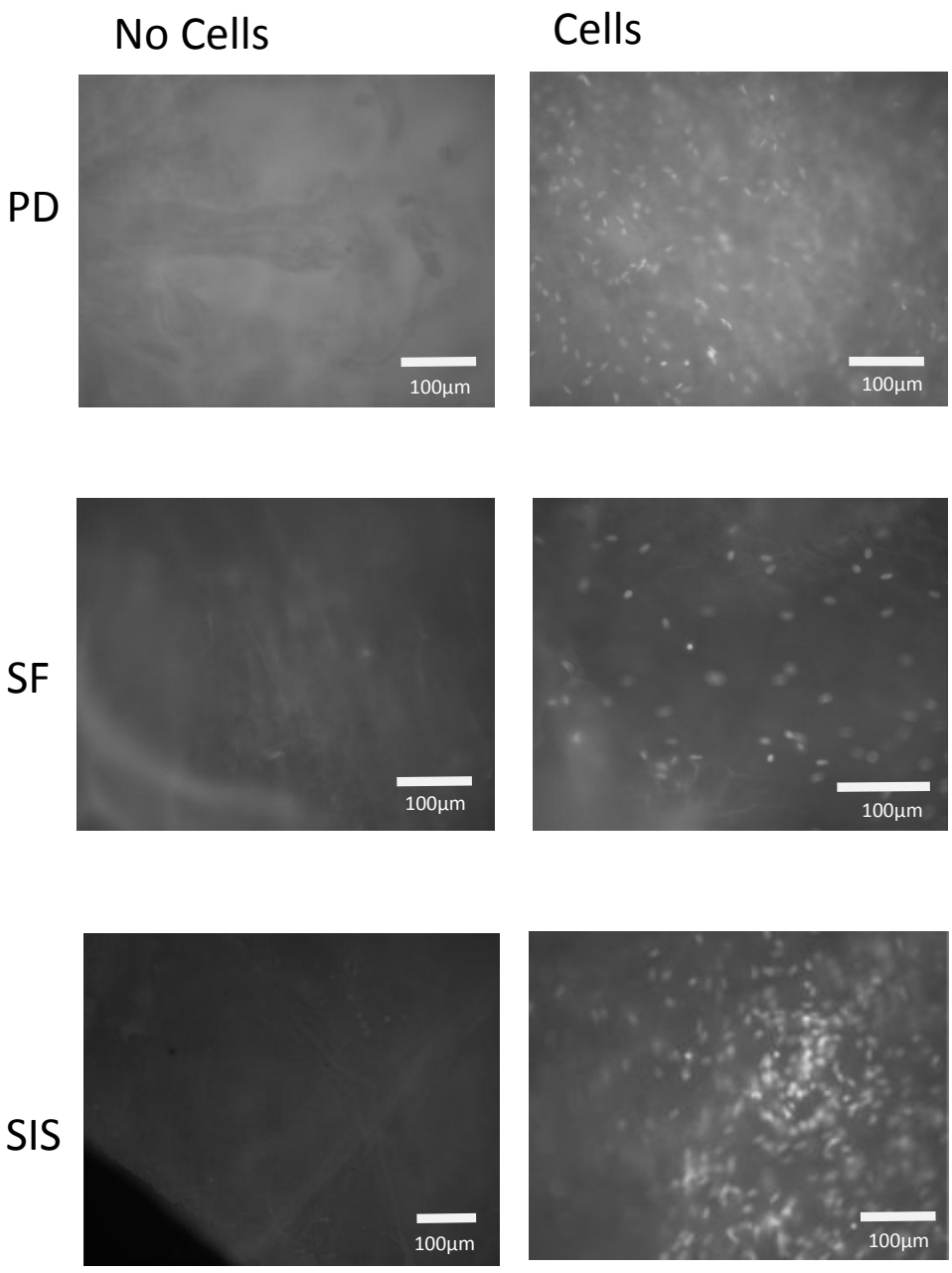

Fig 3.4.1. The distribution of fibroblasts on the seven scaffolds as seen on DAPI stained images.

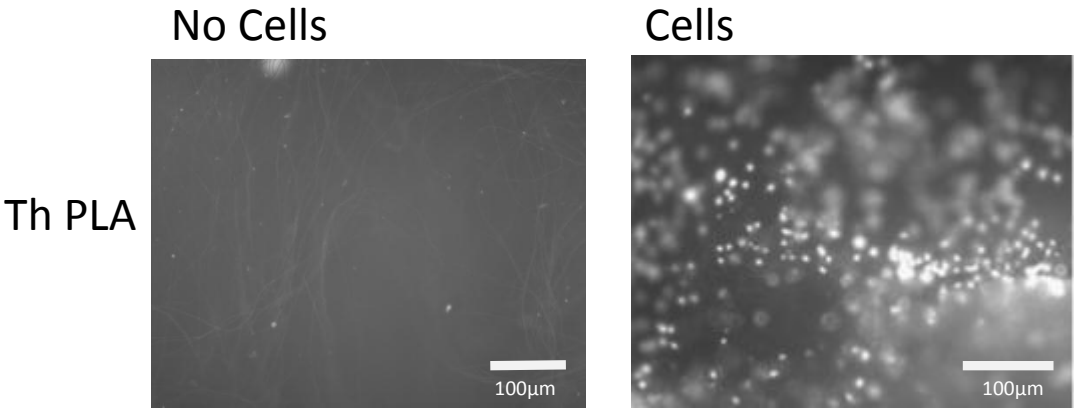

Fig 3.4.1. The distribution of fibroblasts on the seven scaffolds as seen on DAPI stained images.

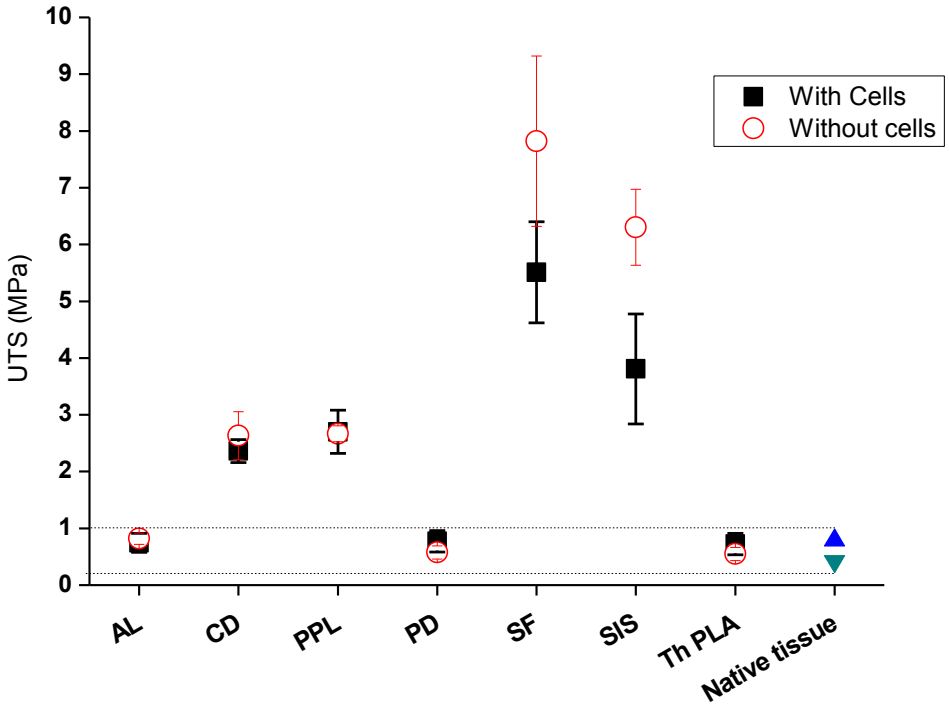

Fig 4.3.1. The ultimate tensile strength of scaffolds with and without cells after 14 days of culture in relation to native tissue, (n=9±SEM), *p<0.05.

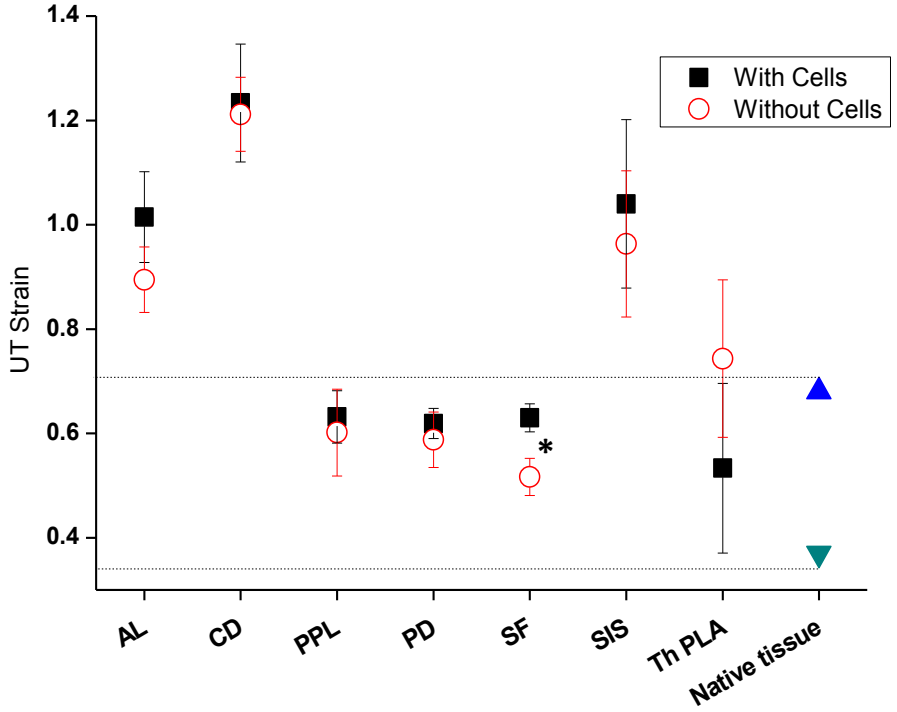

Fig 4.3.2. The ultimate tensile strain of scaffolds with and without cells after 14 days of culture in relation to native tissue, (n=9±SEM), *p<0.05.

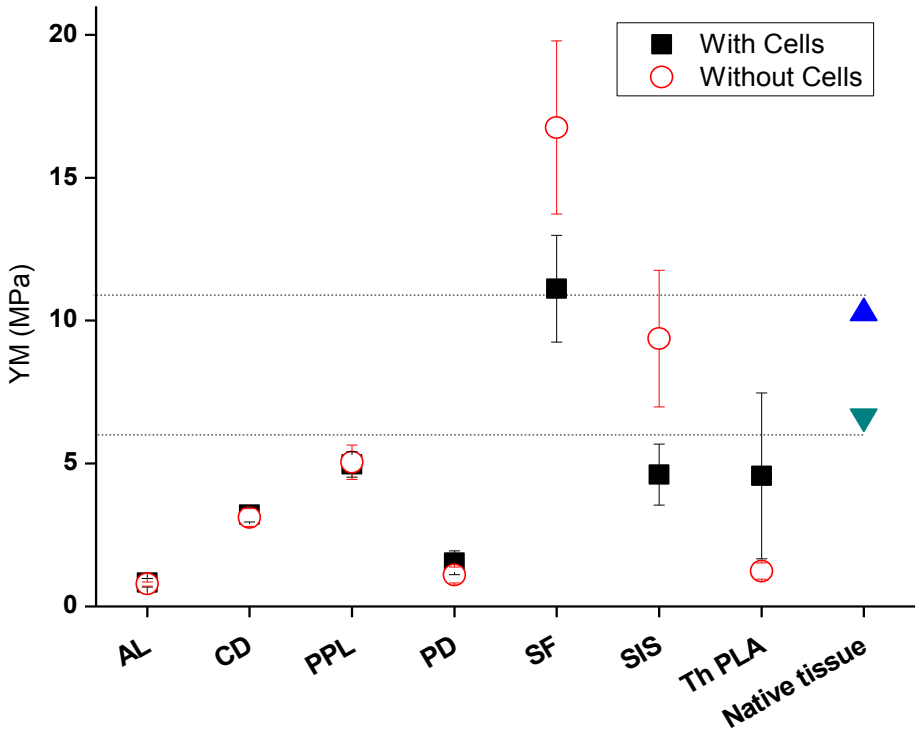

Fig 4.3.3. The Young's modulus of scaffolds with and without cells after 14 days of culture in relation to native tissue, (n=9±SEM), *p<0.05.

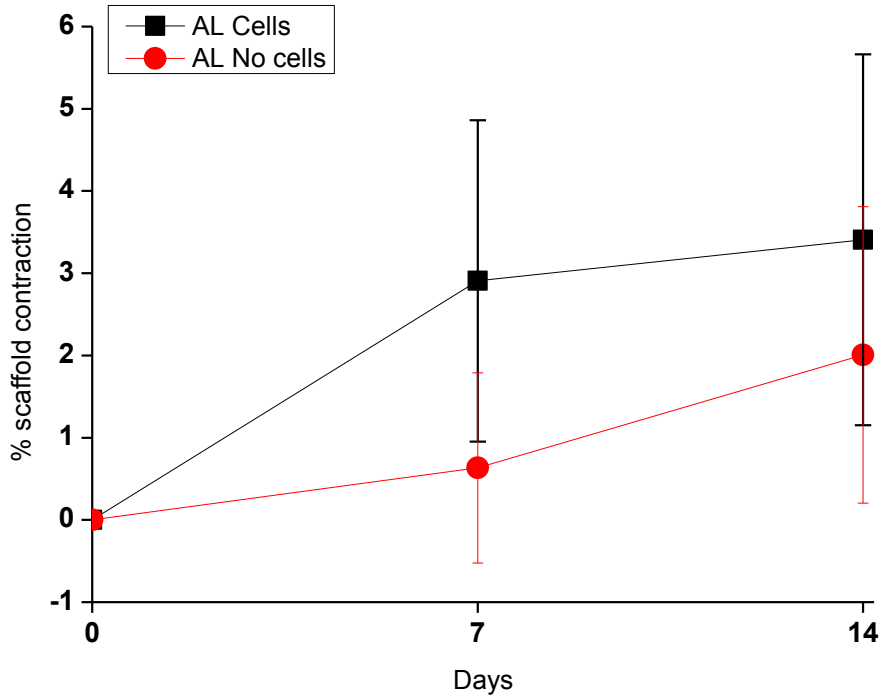

Fig 5.2.1. % contraction of AL with and without cells after 14 days of culture, (n=9±SEM), *p<0.05.

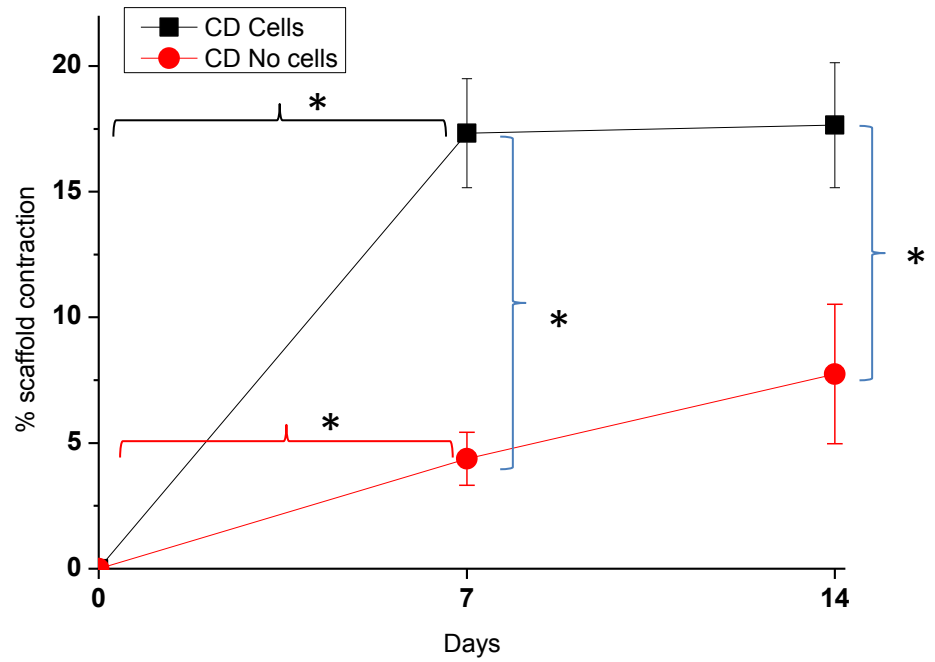

Fig 5.2.2. % contraction of CD with and without cells after 14 days of culture, (n=9±SEM), *p<0.05.

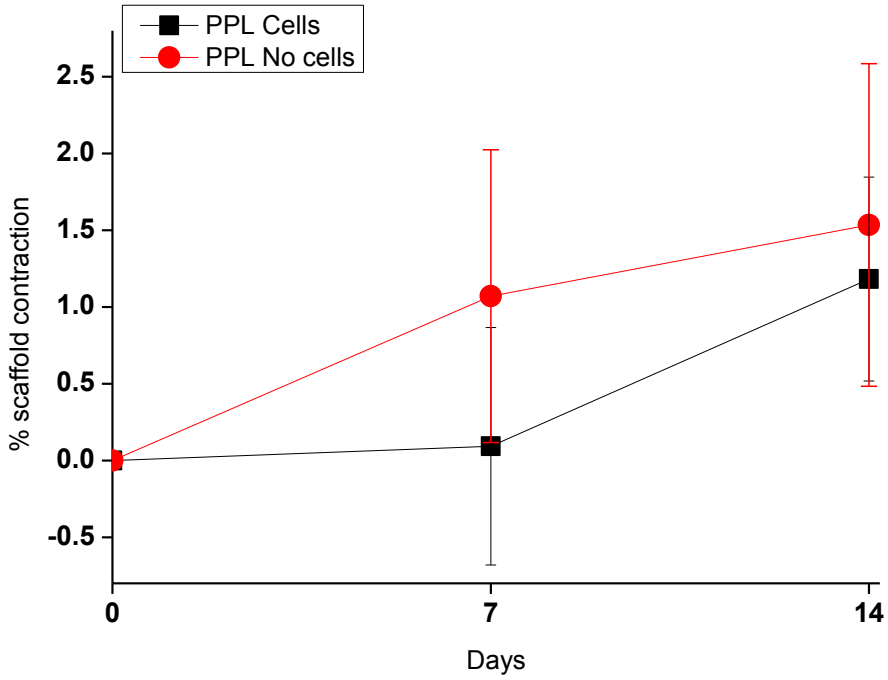

Fig 5.2.3. % contraction of PPL with and without cells after 14 days of culture, (n=9±SEM), *p<0.05.

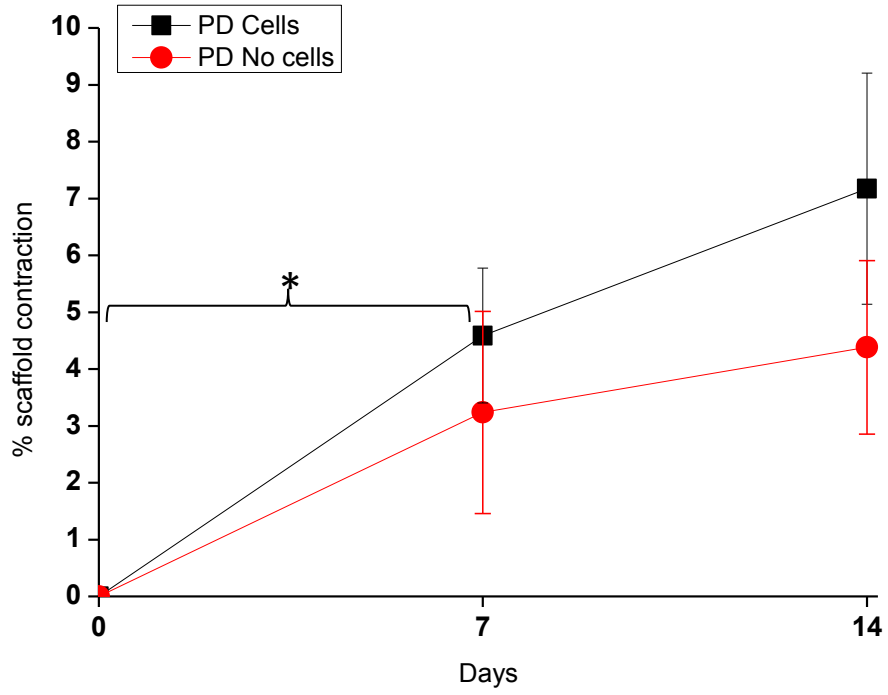

Fig 5.2.4. % contraction of PD with and without cells after 14 days of culture, (n=9±SEM), *p<0.05.

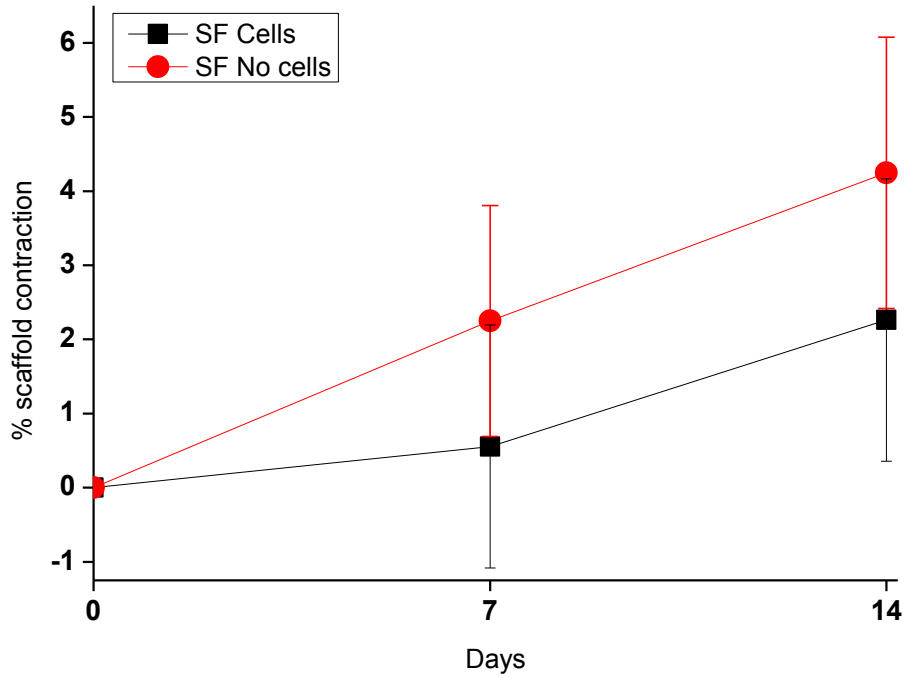

Fig 5.2.5. % contraction of SF with and without cells after 14 days of culture, (n=9±SEM), *p<0.05.

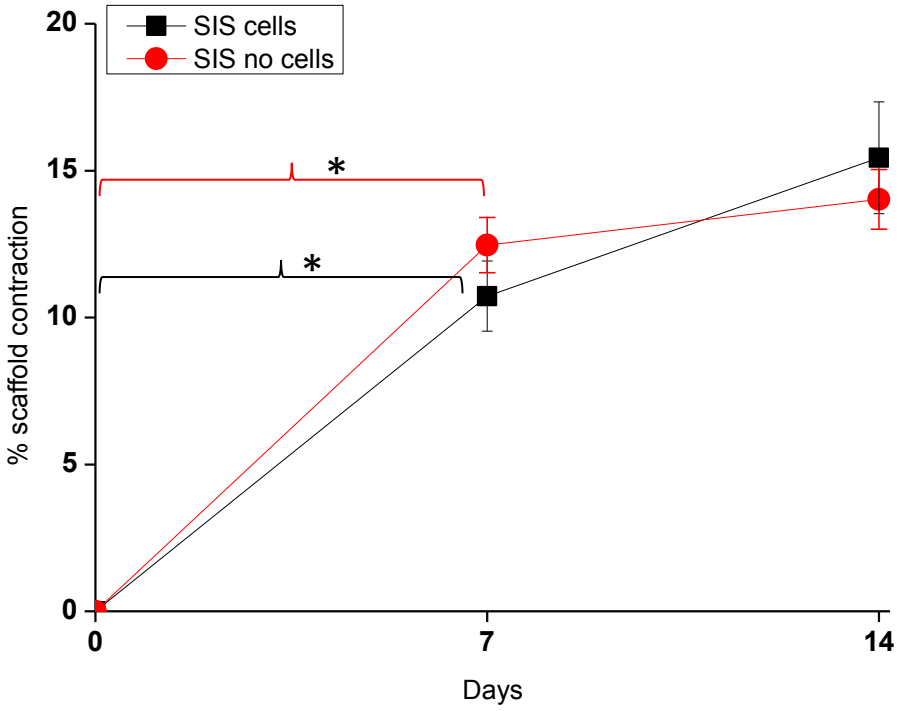

Fig 5.2.6. % contraction of SIS with and without cells after 14 days of culture, (n=9±SEM), *p<0.05.

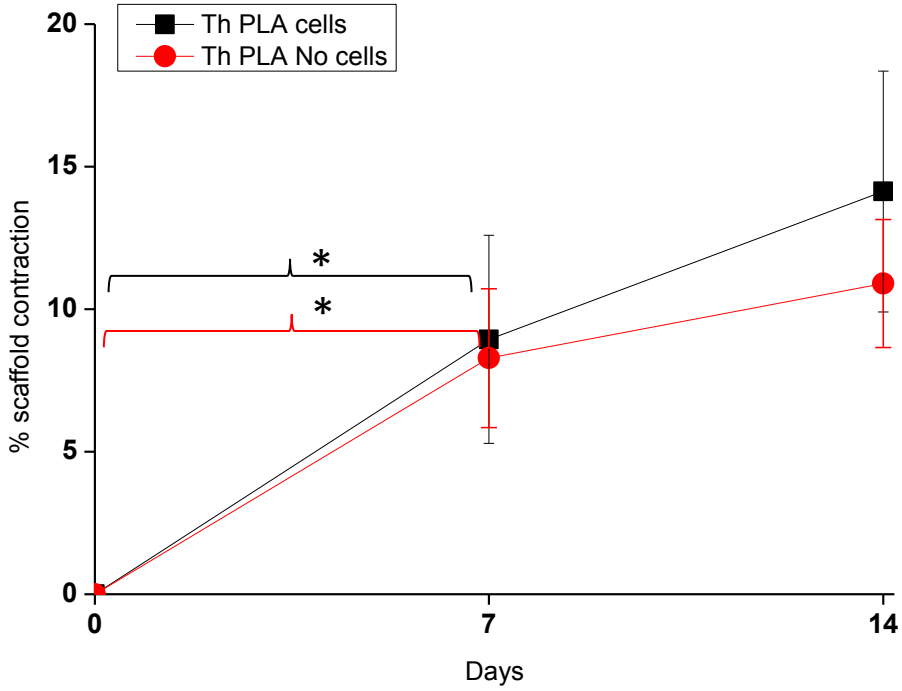

Fig 5.2.7. % contraction of Th PLA with and without cells after 14 days of culture, (n=9±SEM), *p<0.05.

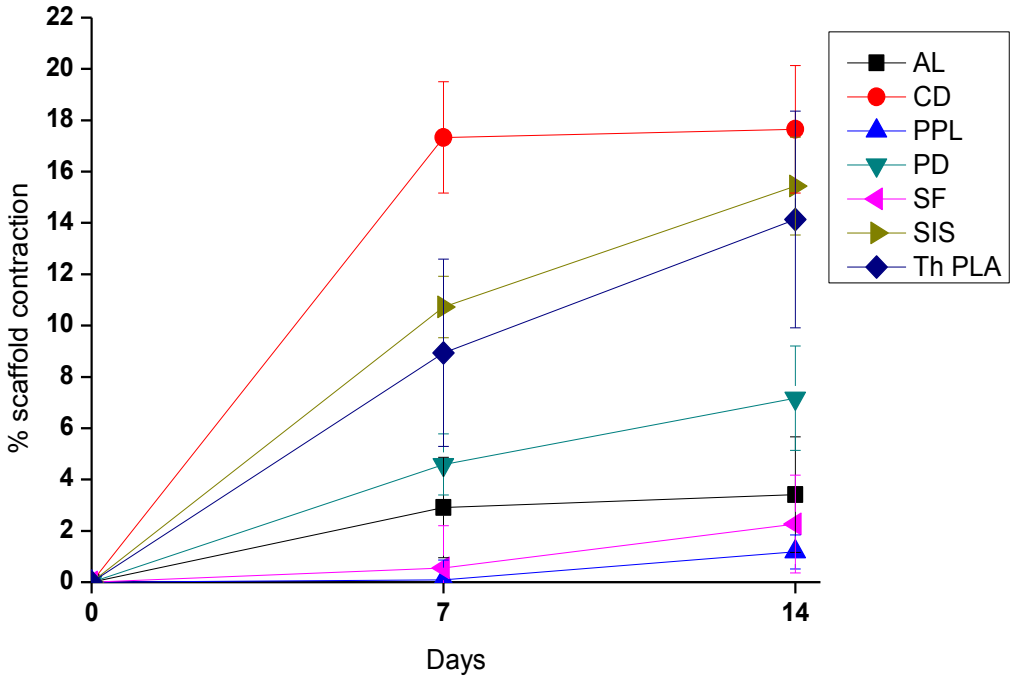

Fig 5.3.1. % contraction of all scaffolds with cells after 14 days of culture, (n=9±SEM).

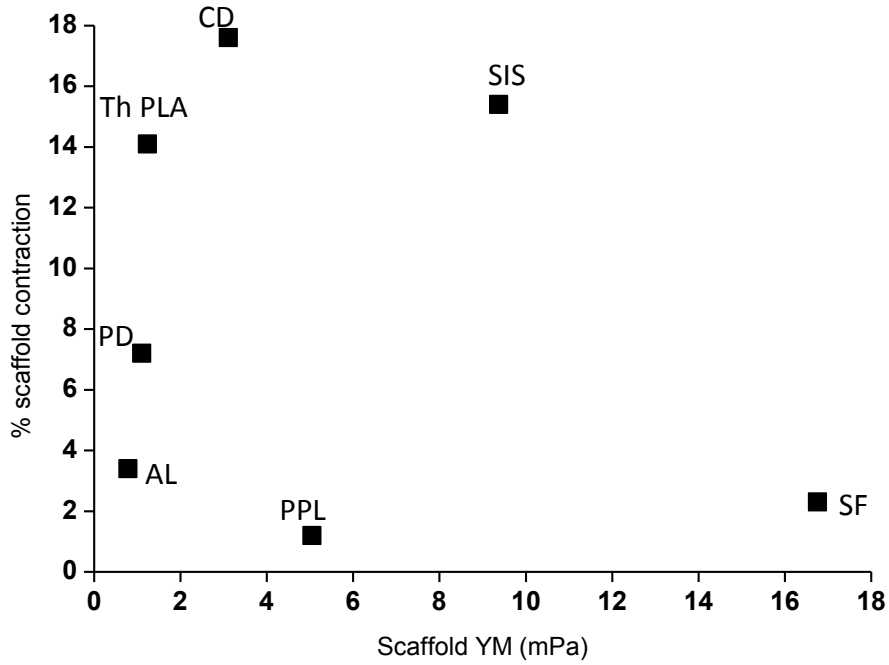

Fig 5.3.2.Correlation of scaffold contraction at 14 days with YM, (n=9).

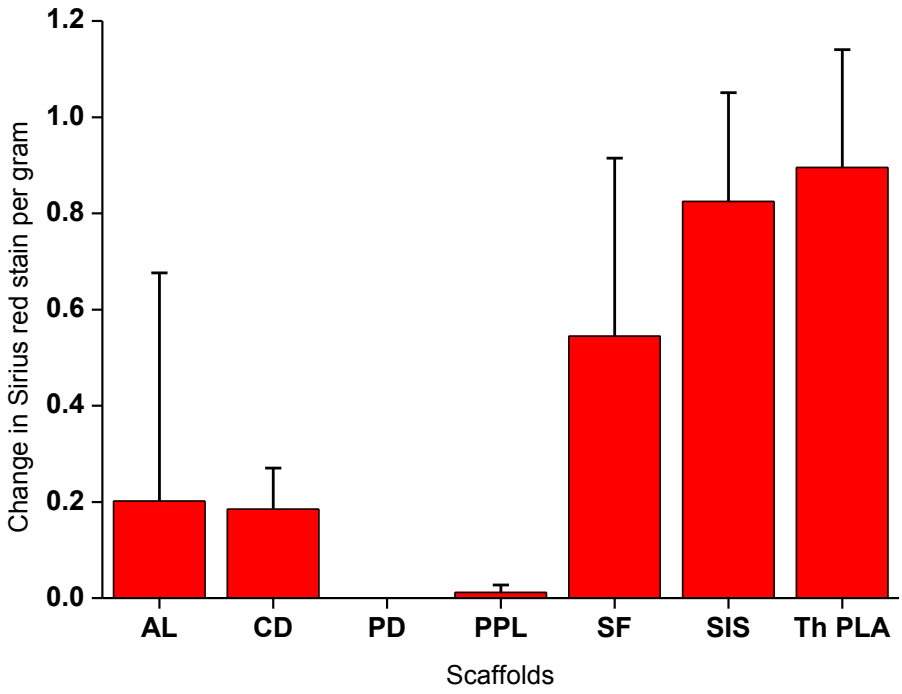

Fig 6.2.1. Collagen production by cells on scaffolds as assessed by absorbance of Sirius red stain per gram of scaffold. (n=9±SEM).

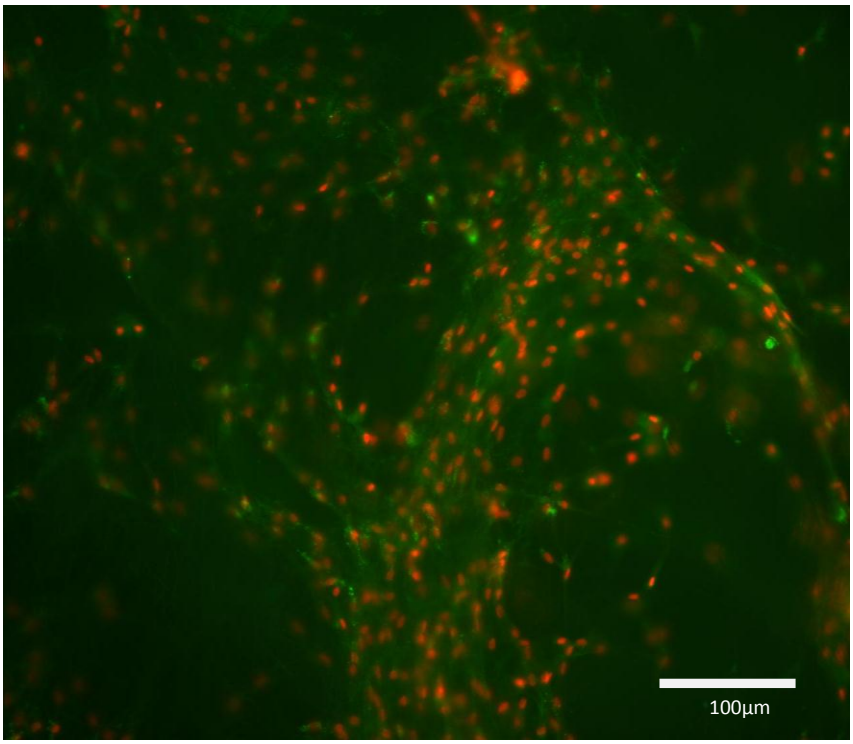

Fig 6.3.1a. DAPI stained nuclei (red), FITC labelled collagen I (green) on Th PLA scaffold.

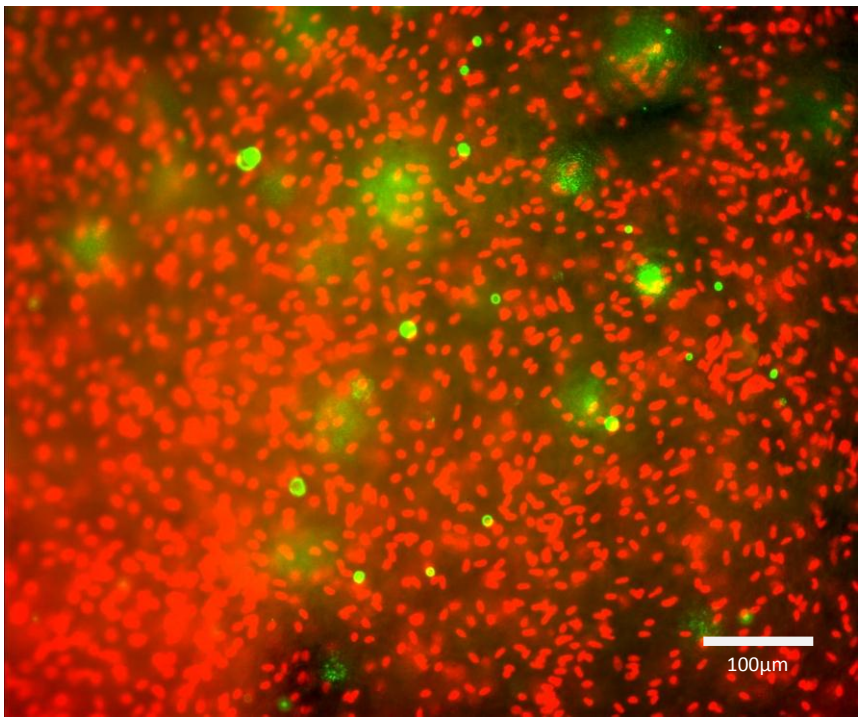

Fig 6.3.1b. DAPI stained nuclei (red), FITC labelled collagen III (green) on Th PLA scaffold.

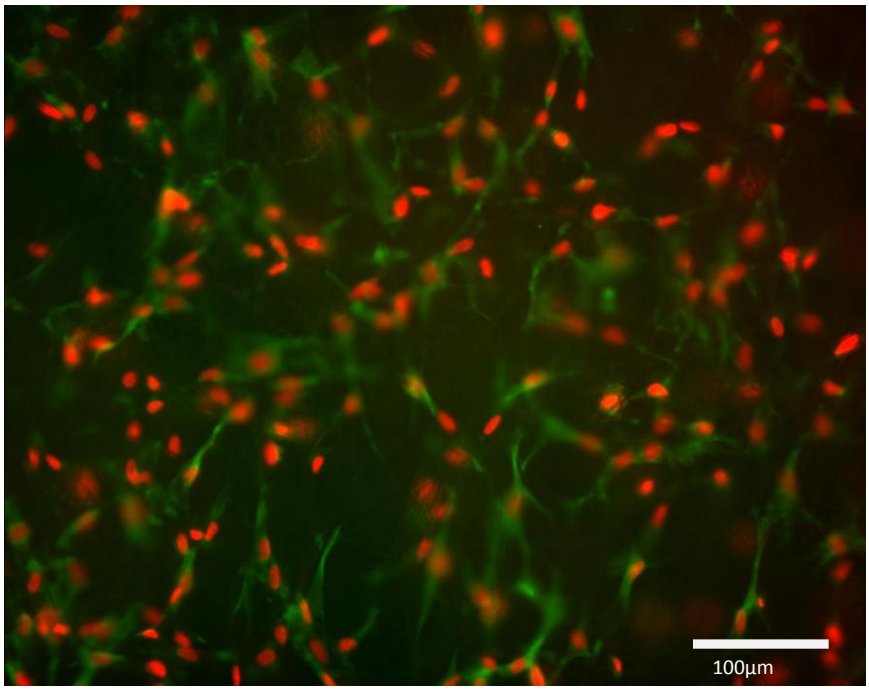

Fig 6.3.1c. DAPI stained nuclei (red), FITC labelled elastin (green) on Th PLA scaffold.

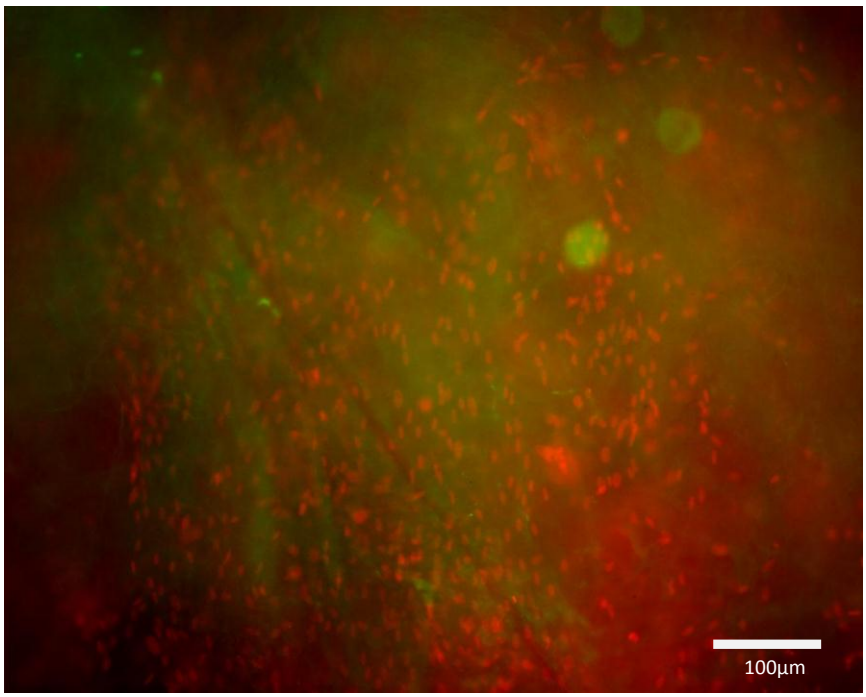

Fig 6.3.2a. DAPI stained nuclei (red), FITC labelled collagen I (green) on SIS scaffold.

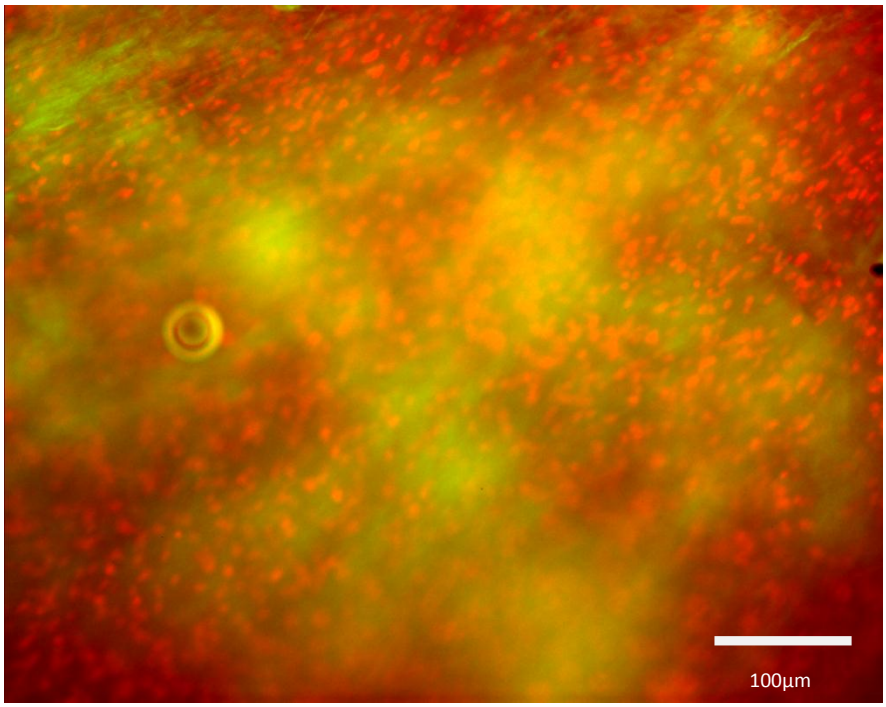

Fig 6.3.2b. DAPI stained nuclei (red), FITC labelled collagen III (green) on SIS scaffold.

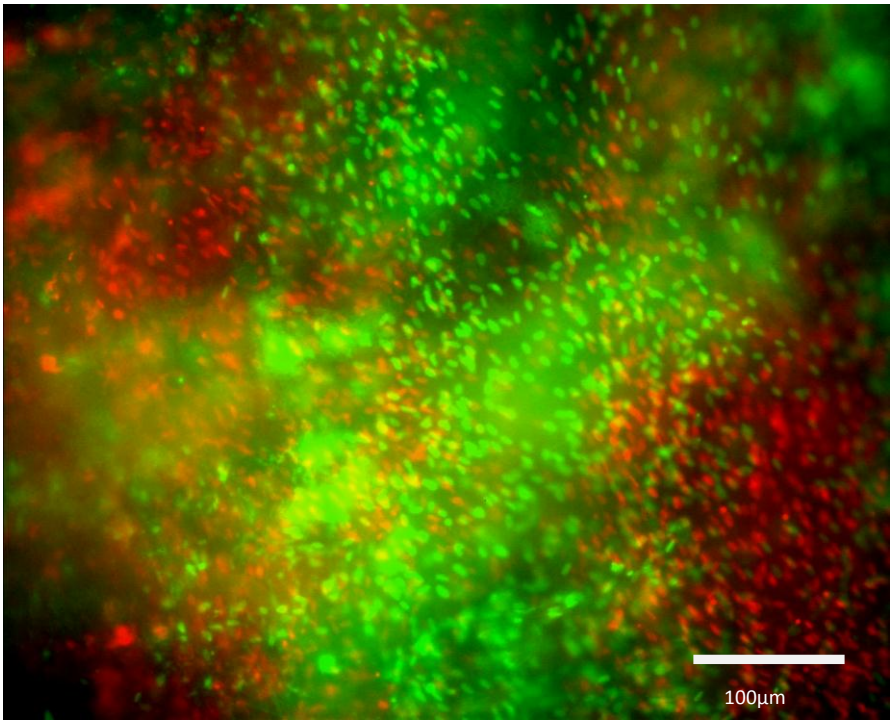

Fig 6.3.2c. DAPI stained nuclei (red), FITC labelled elastin (green) on SIS scaffold.

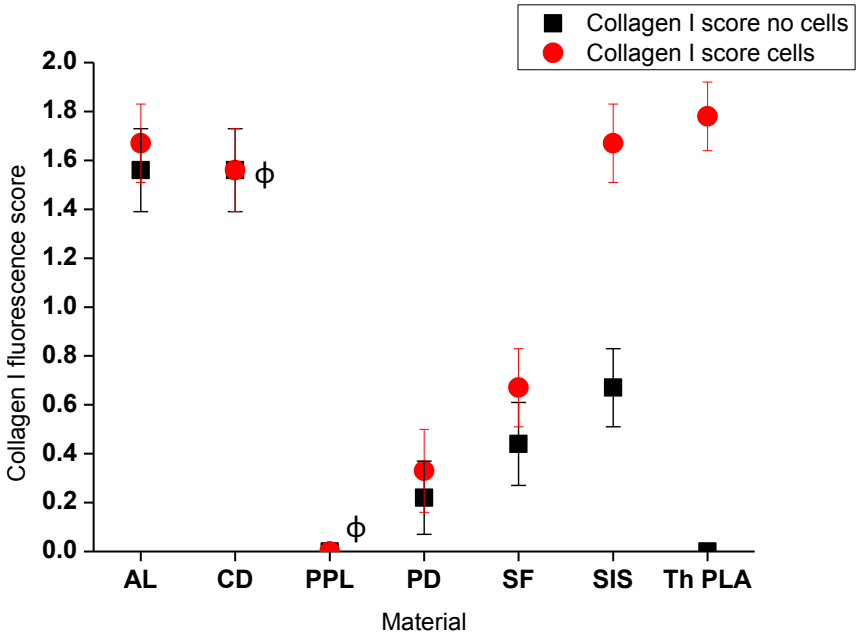

Fig 6.3.3. Collagen I on scaffolds as assessed by three independent assessors of fluorescence stained images (n=9±SEM). 0= no fluorescence, 1= mild fluorescence, 2=good fluorescence, 3= abundant fluorescence.Φ= Overlapping symbols.

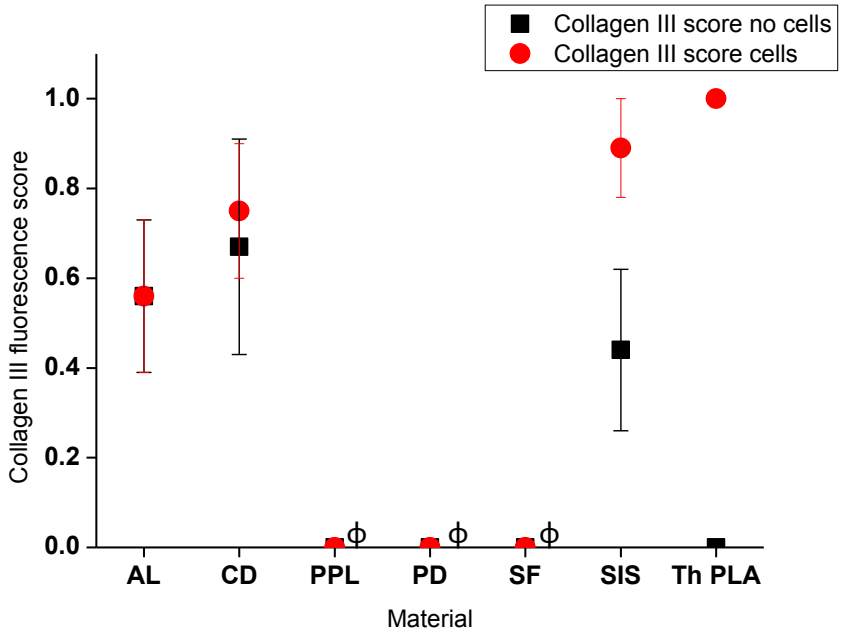

Fig 6.3.4. Collagen III on scaffolds as assessed by three independent assessors of fluorescence stained images (n=9±SEM). 0= no fluorescence, 1= mild fluorescence, 2=good fluorescence, 3= abundant fluorescence. Φ=Overlapping symbols.

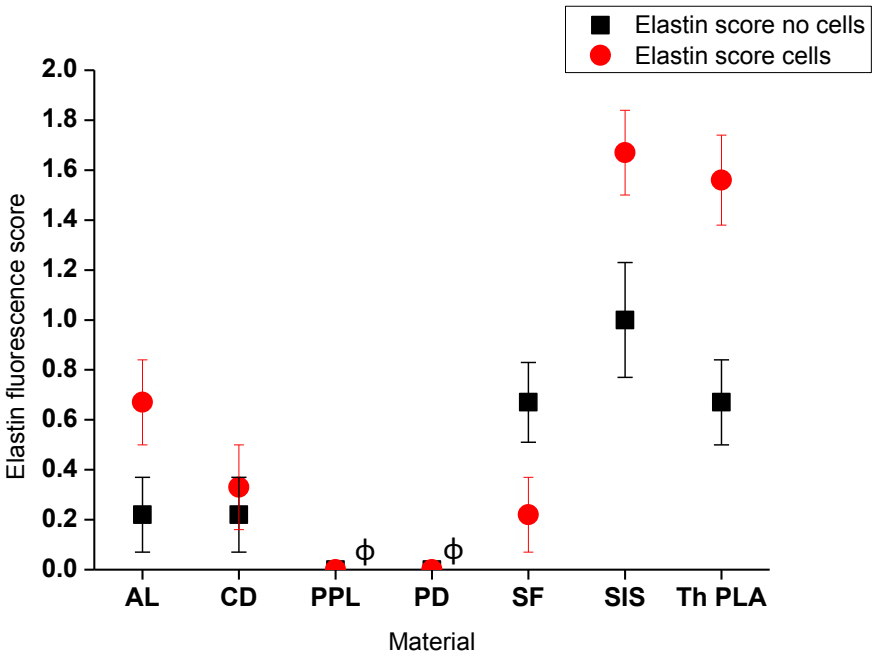

Fig 6.3.5. Elastin on scaffolds as assessed by three independent assessors of fluorescence stained images (n=9±SEM). 0= no fluorescence, 1= mild fluorescence, 2= good fluorescence, 3= abundant fluorescence. Φ= Overlapping symbols.

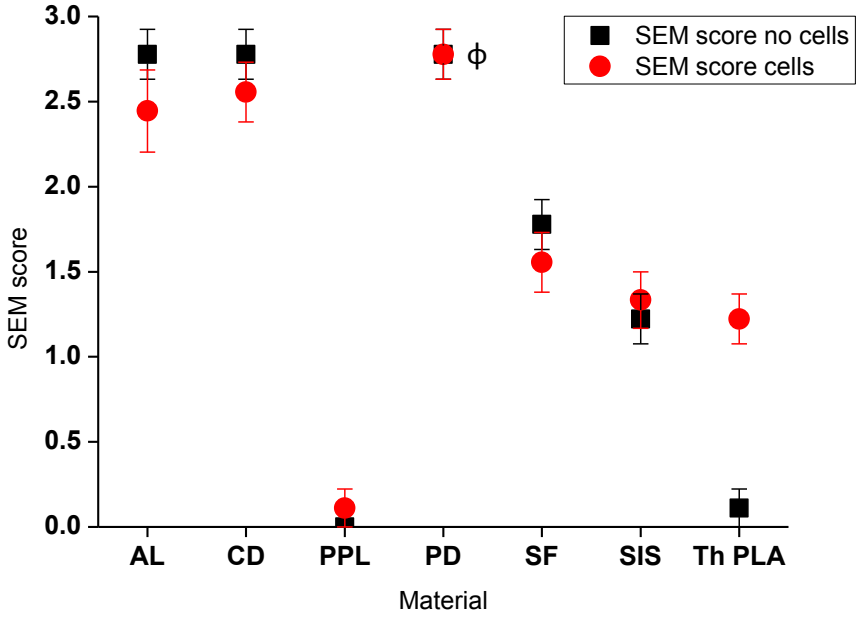

Fig 6.4.1. ECM on scaffolds as assessed by three independent assessors of SEM images (n=9±SEM). 0= no ECM, 1= little ECM, 2= good ECM, 3= abundant ECM. Φ= Overlapping symbols.

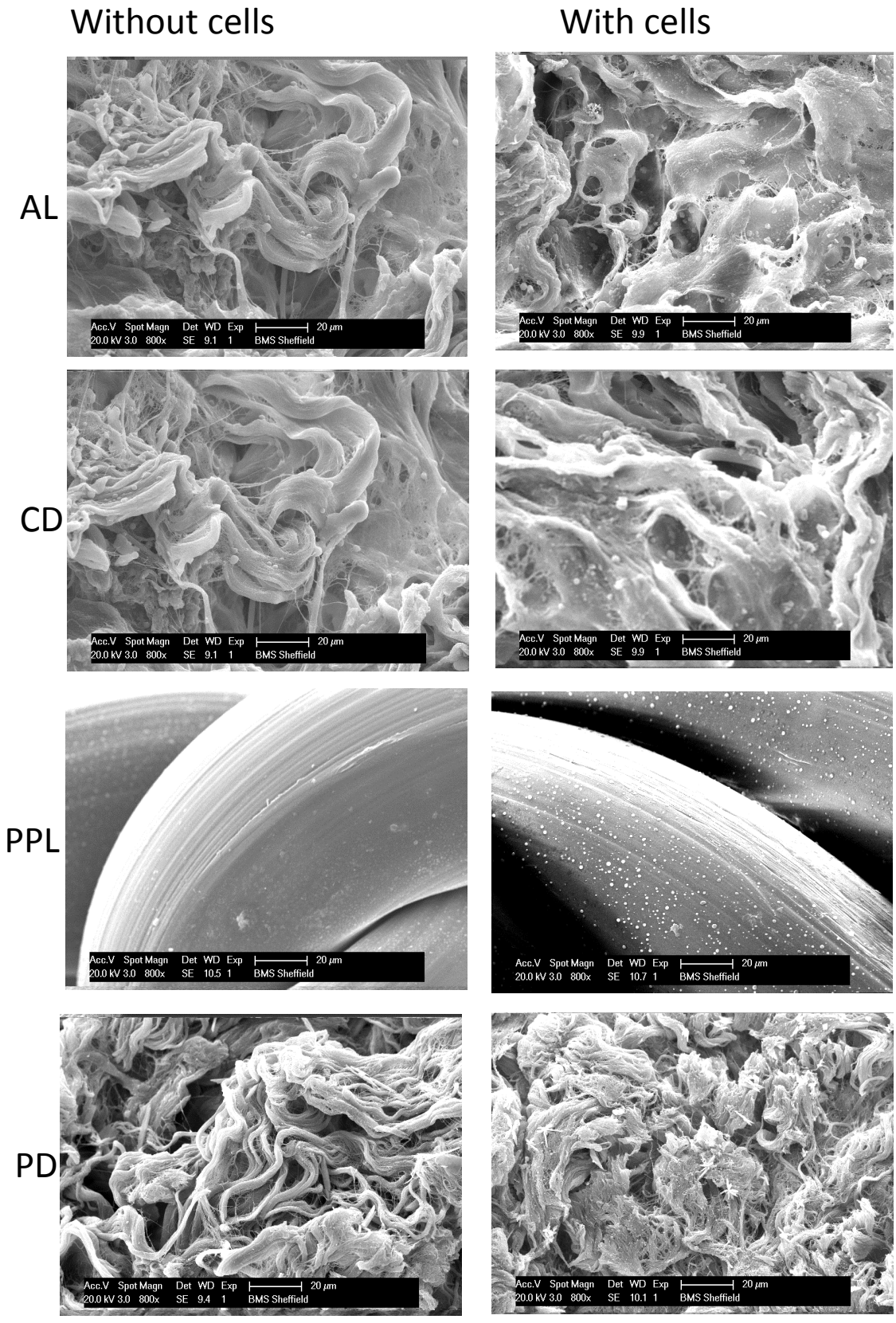

Fig 6.4.2. Representative SEM images of scaffolds with and without cells.

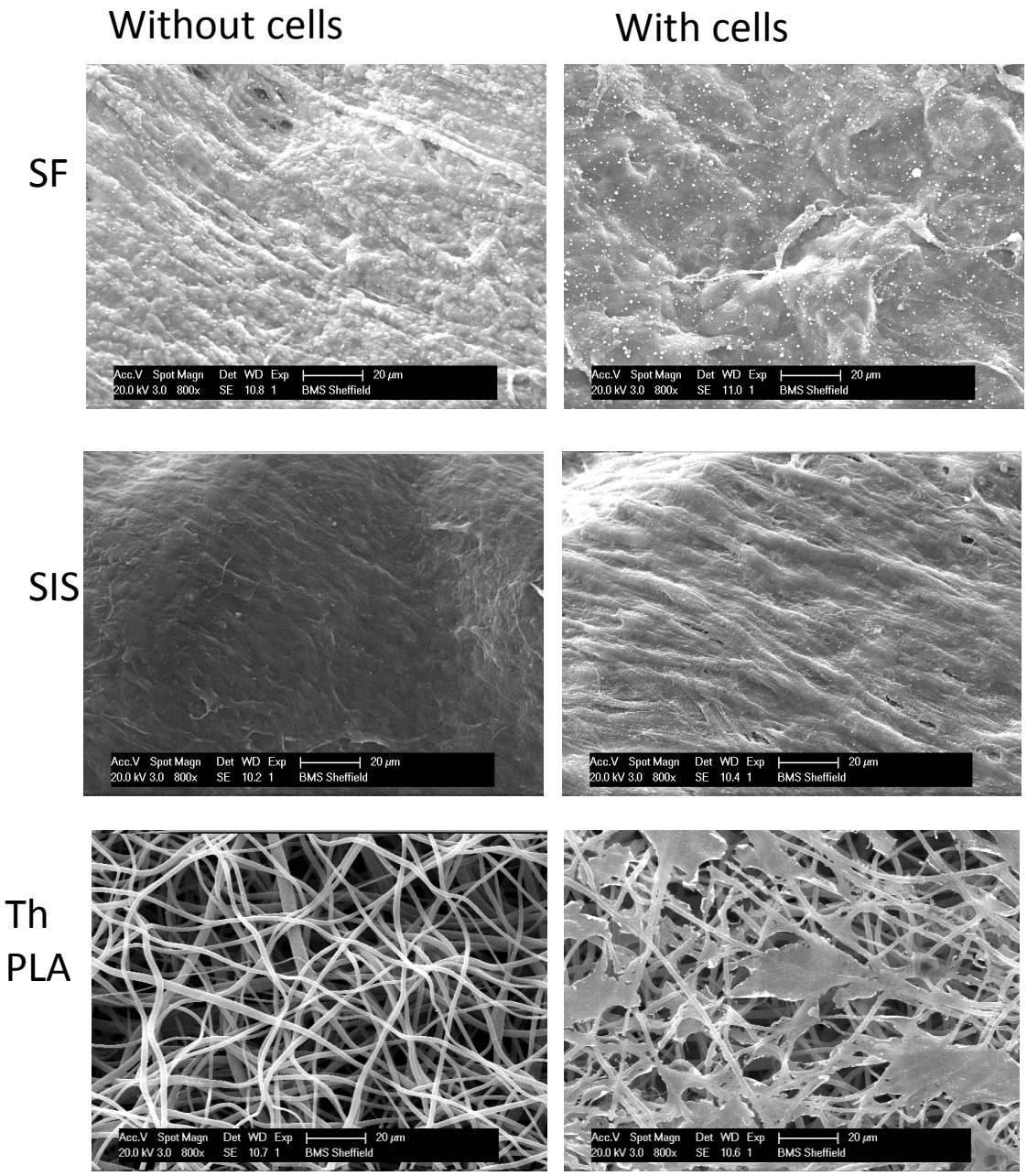

Fig 6.4.2. Representative SEM images of scaffolds with and without cells.

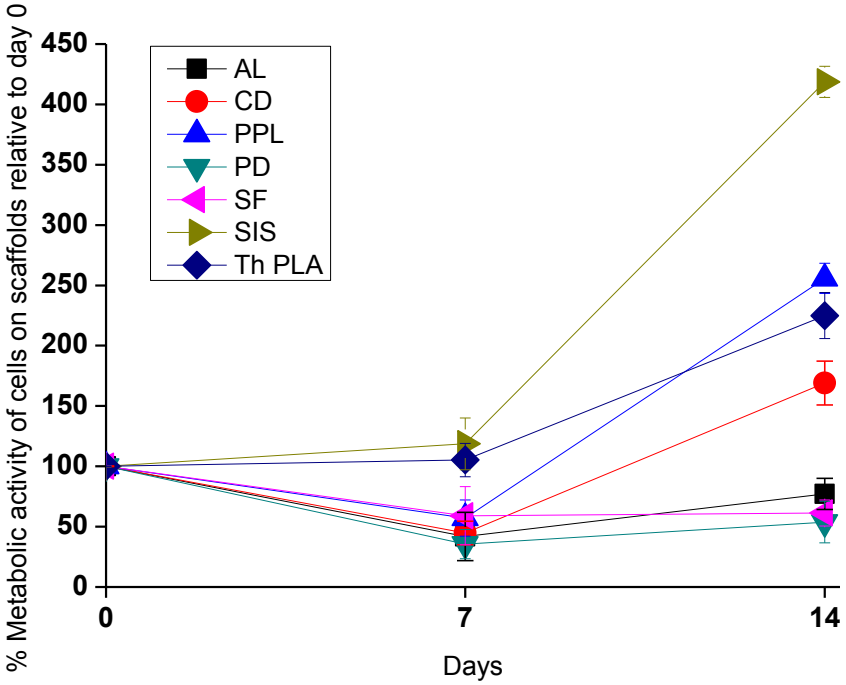

Fig 7.2.1.1. The metabolic activity of fibroblasts on the seven restrained scaffolds, as assessed by absorbance of AlamarBlue stain at 570nm over 14 days, (n=9±SEM).

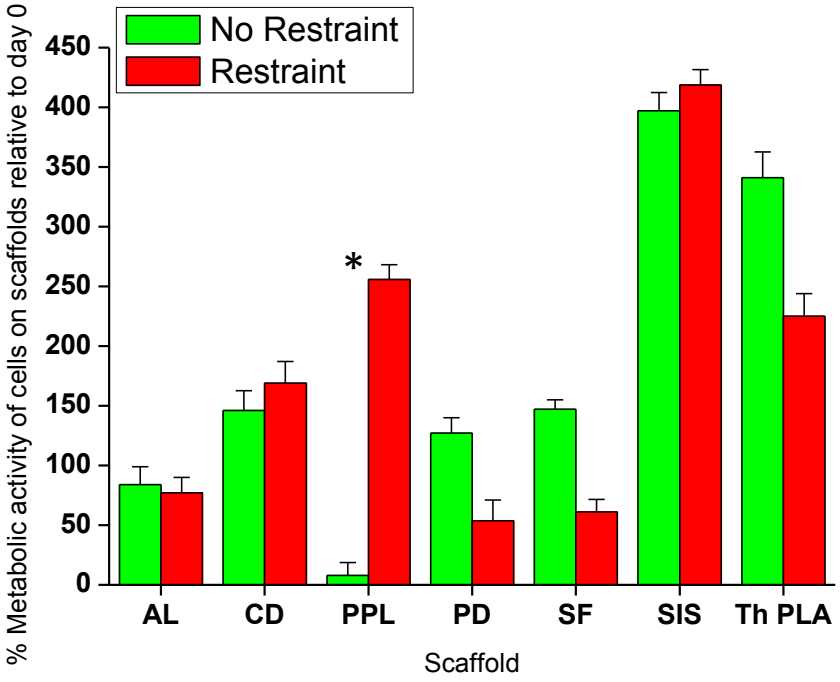

Fig 7.2.1.2. The metabolic activity of fibroblasts on the seven restrained and unrestrained scaffolds, as assessed by absorbance of AlamarBlue stain at 570nm at 14 days, (n=9±SEM), *p<0.05.

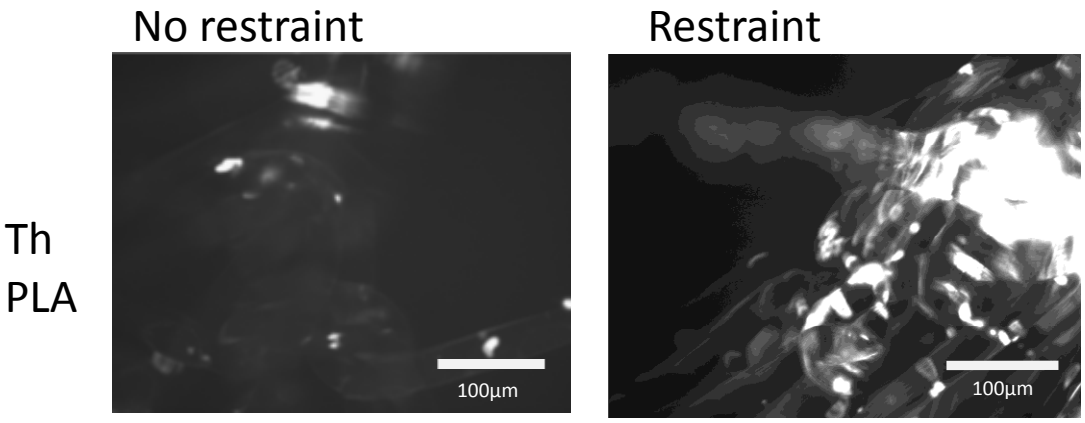

Fig 7.2.1.3. The distribution of fibroblasts on restrained and unrestrained PPL as seen on DAPI stained images.

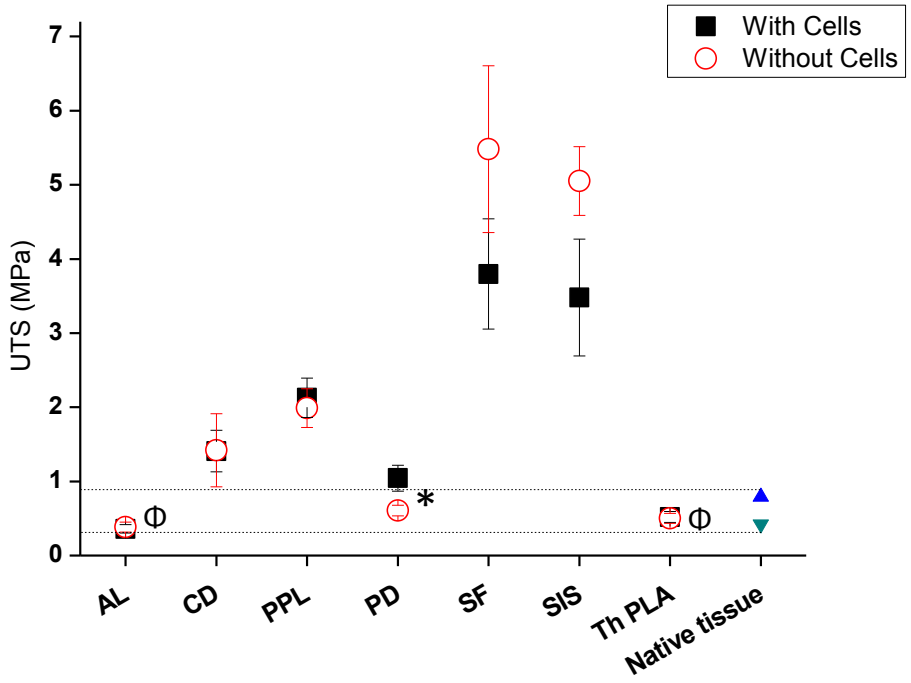

Fig 7.2.2.1. The ultimate tensile strength of restrained scaffolds with and without cells after 14 days of culture in relation to native tissue, (n=9±SEM), *p<0.05. Φ= Overlapping symbols

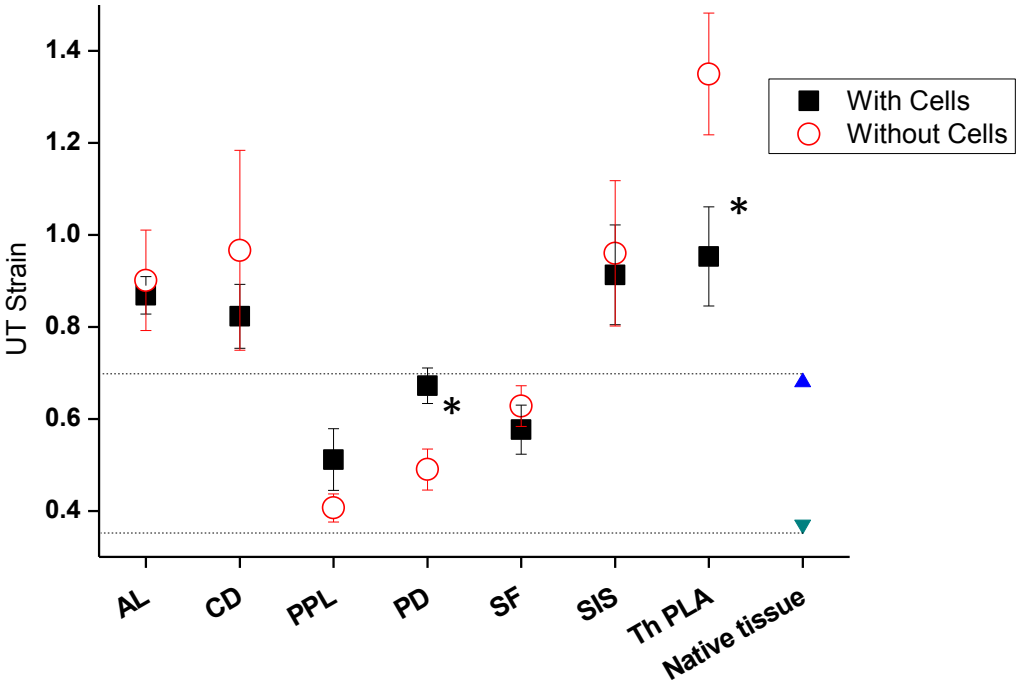

Fig 7.2.2.2. The ultimate tensile strain of restrained scaffolds with and without cells after 14 days of culture in relation to native tissue, (n=9±SEM), *p<0.05.

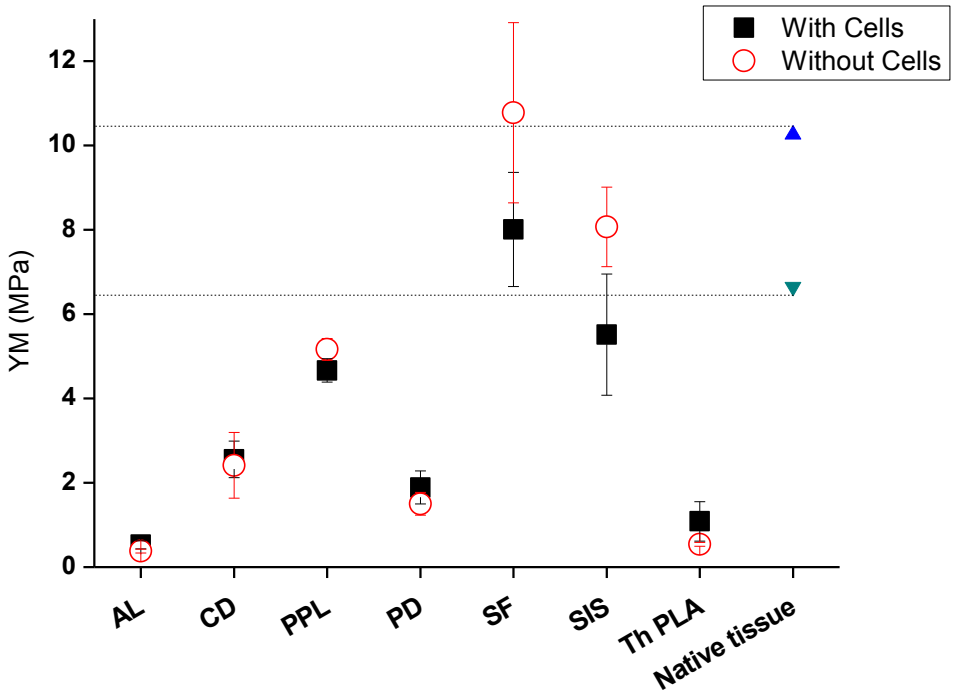

Fig 7.2.2.3. The Young's modulus of restrained scaffolds with and without cells after 14 days of culture in relation to native tissue, (n=9±SEM), *p<0.05.

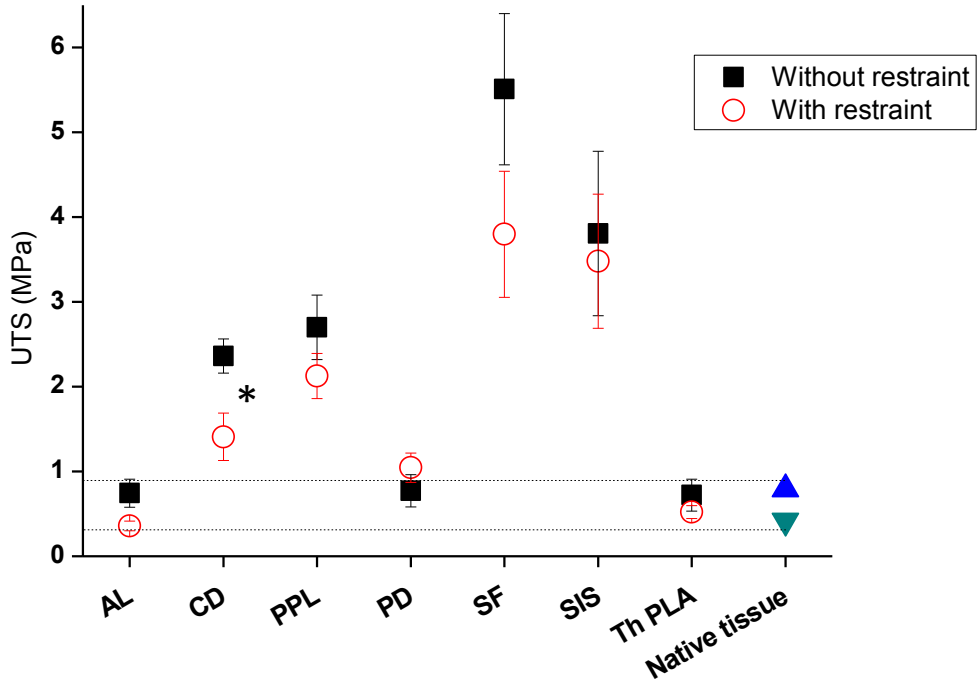

Fig 7.2.2.4. The ultimate tensile strength of restrained and unrestrained scaffolds with cells after 14 days of culture in relation to native tissue, (n=9±SEM), *p<0.05.

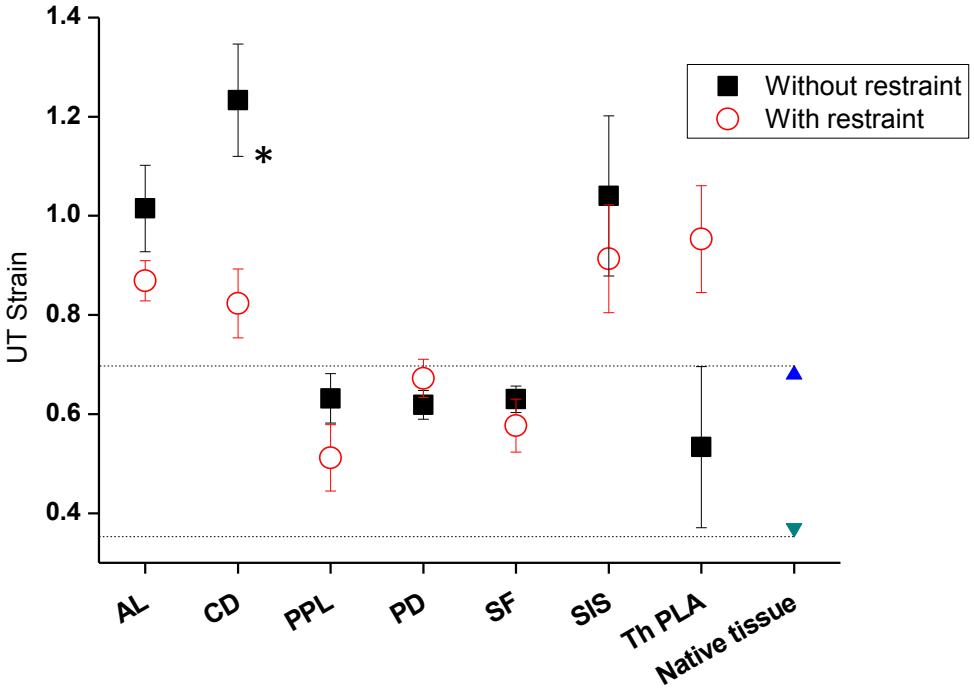

Fig 7.2.2.5. The ultimate tensile strain of restrained and unrestrained scaffolds with cells after 14 days of culture in relation to native tissue, (n=9±SEM), *p<0.05.

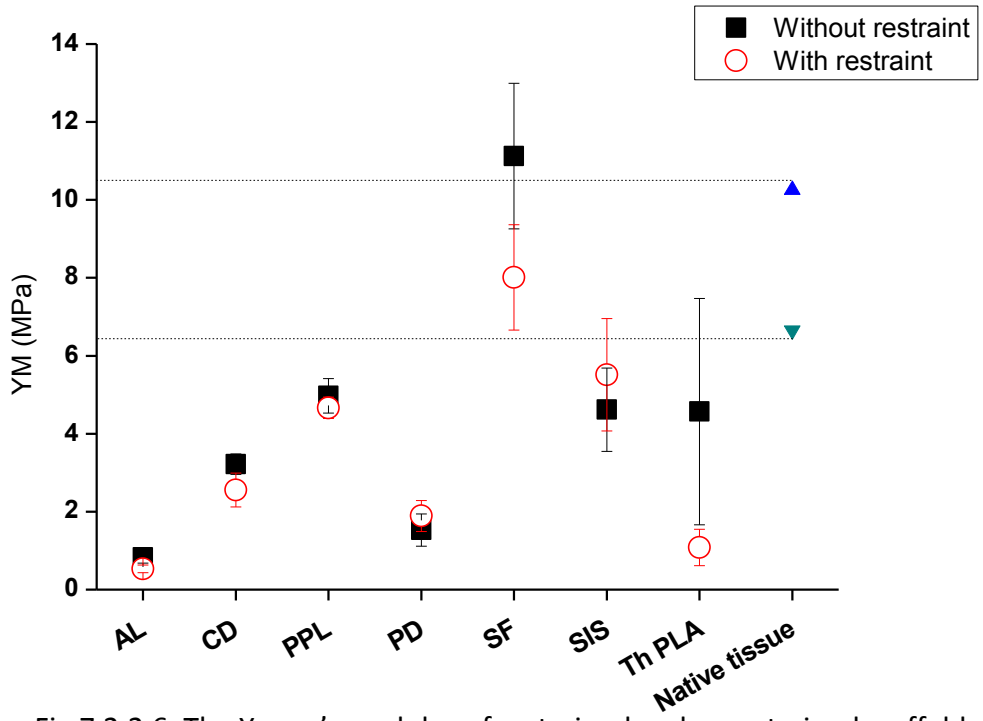

Fig 7.2.2.6. The Young's modulus of restrained and unrestrained scaffolds with cells after 14 days of culture in relation to native tissue, (n=9±SEM), *p<0.05.

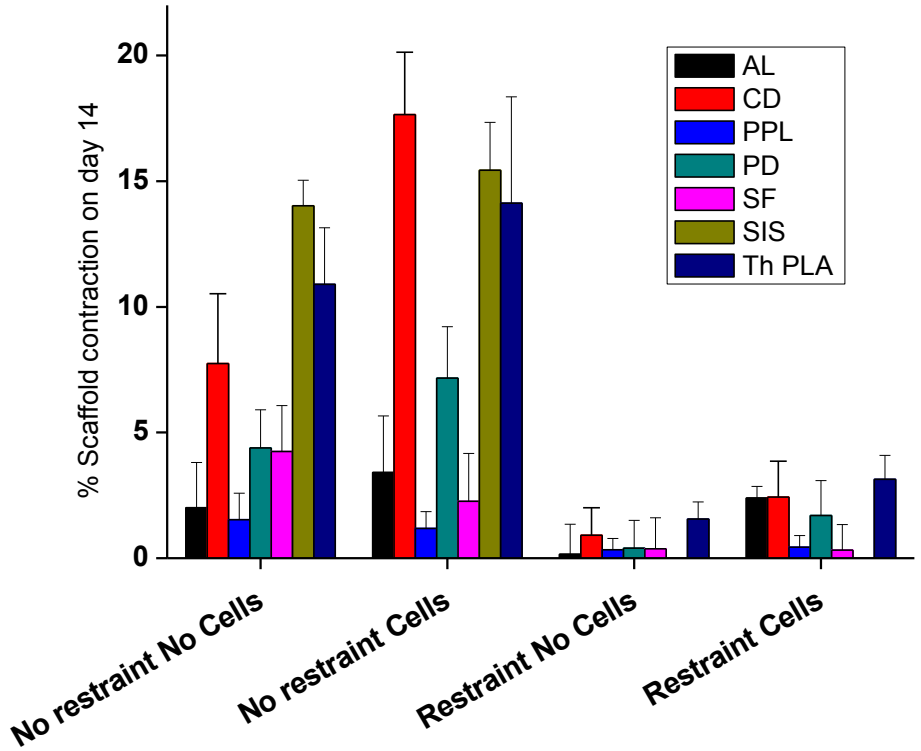

Fig 7.2.3.1. The % contraction of restrained and unrestrained scaffolds with and without cells after 14 days of culture.

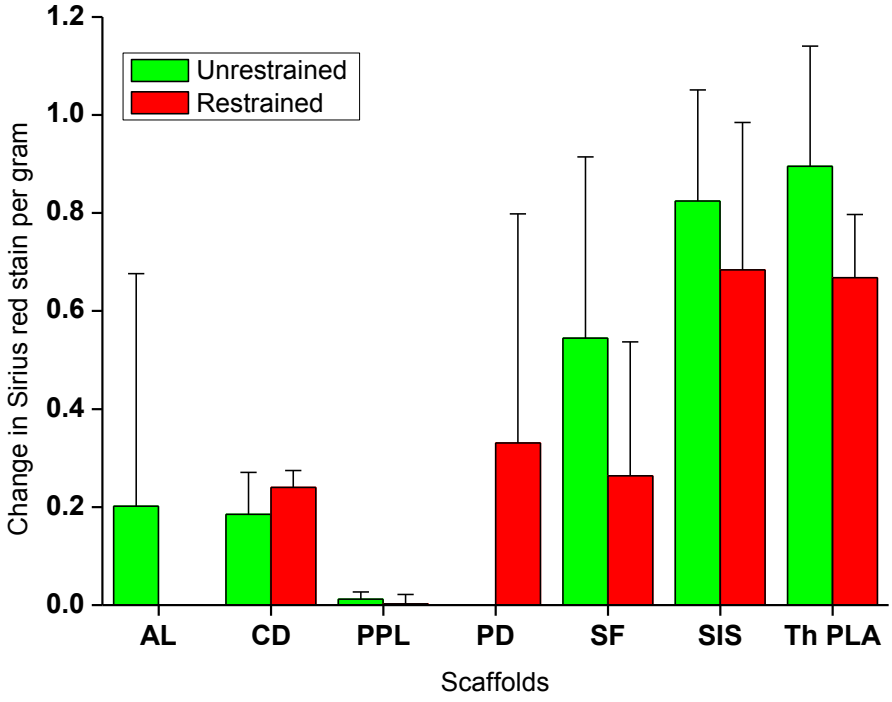

Fig 7.2.4.1.1 Collagen production by cells on scaffolds as assessed by absorbance of Sirius red stain per gram of scaffold, (n=9±SEM), *p<0.05.

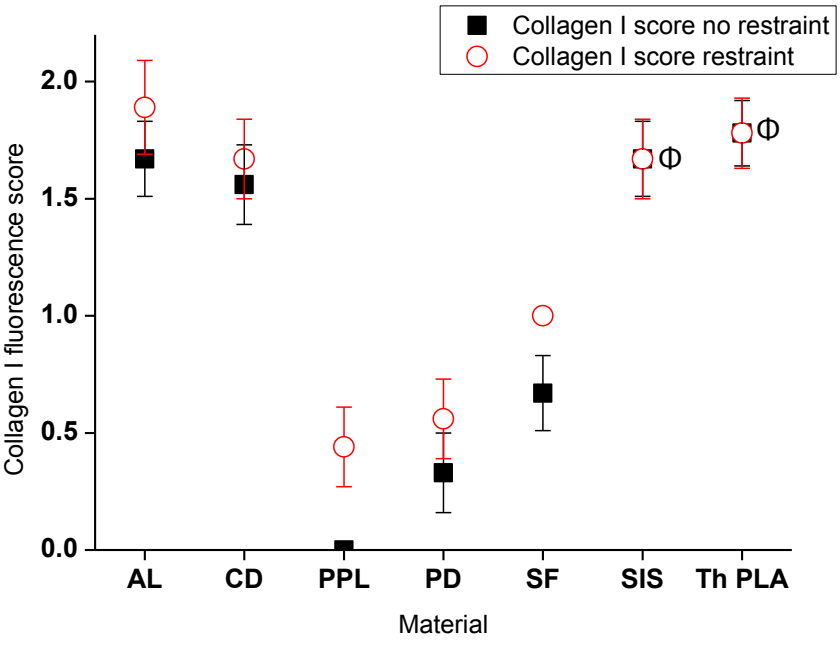

Fig 7.2.4.2.1 Collagen I on restrained and unrestrained scaffolds as assessed by three independent assessors of fluorescence stained images (n=9±SEM), 0= no fluorescence, 1= mild fluorescence, 2=good fluorescence, 3= abundant fluorescence. Φ= Overlapping symbols

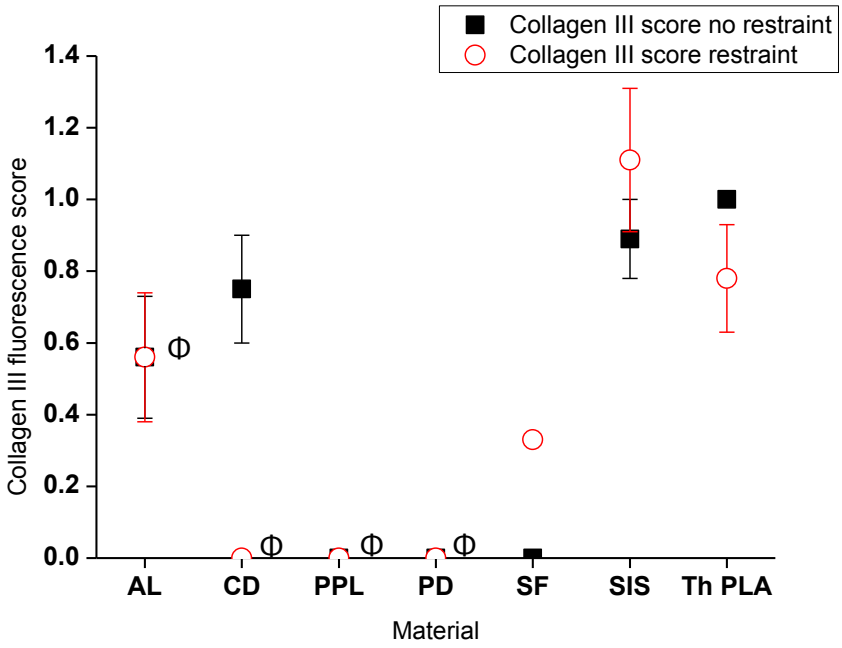

Fig 7.2.4.2.2. Collagen III on restrained and unrestrained scaffolds as assessed by three independent assessors of fluorescence stained images (n=9±SEM). 0= no fluorescence, 1= mild fluorescence, 2=good fluorescence, 3= abundant fluorescence. Φ= Overlapping symbols

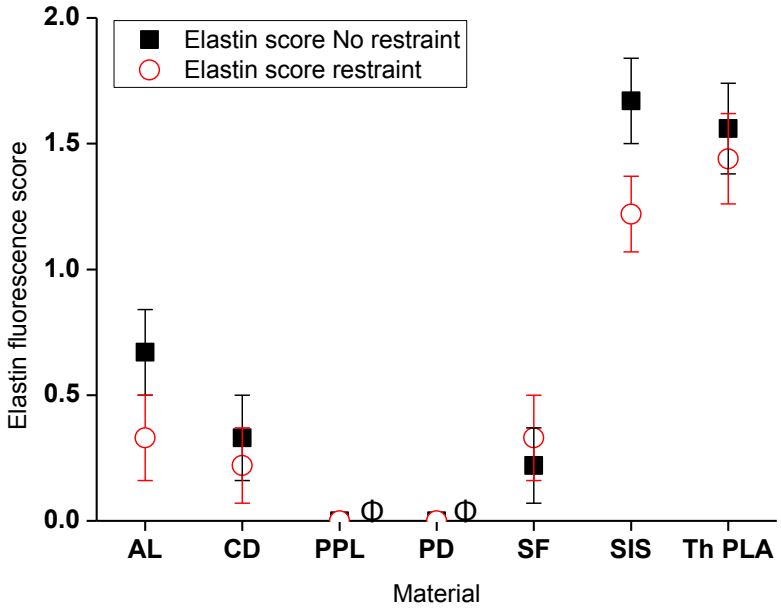

Fig 7.2.4.2.3. Elastin on restrained and unrestrained scaffolds as assessed by three independent assessors of fluorescence stained images (n=9±SEM). 0= no fluorescence, 1= mild fluorescence, 2=good fluorescence, 3= abundant fluorescence. Φ= Overlapping symbols.

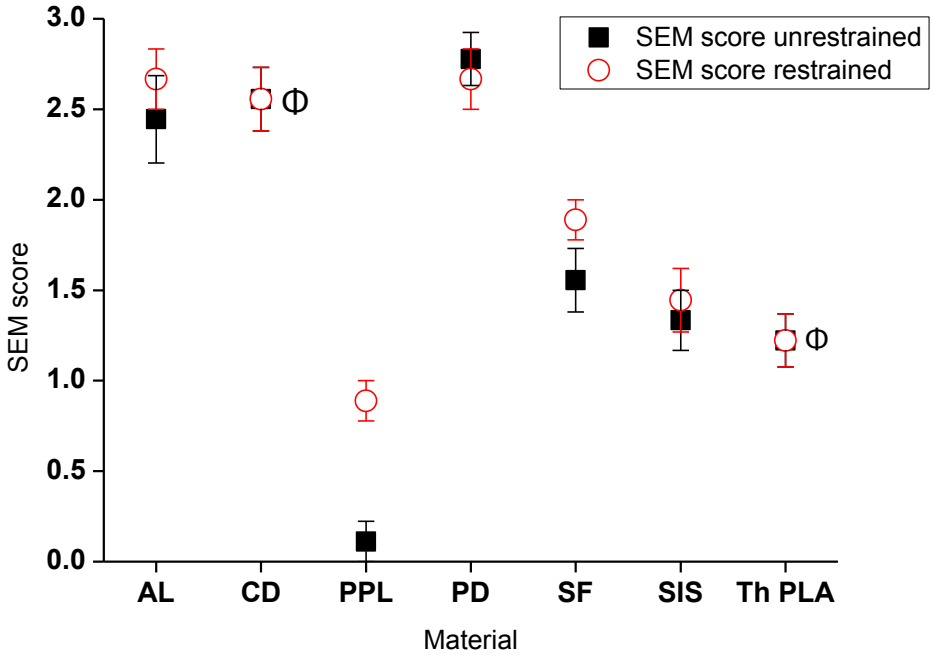

Fig 7.2.4.3.1. ECM on restrained and unrestrained scaffolds as assessed by three independent assessors of SEM images (n=9±SEM). 0= no ECM, 1= little ECM, 2= good ECM, 3= abundant ECM. Φ= Overlapping symbols.

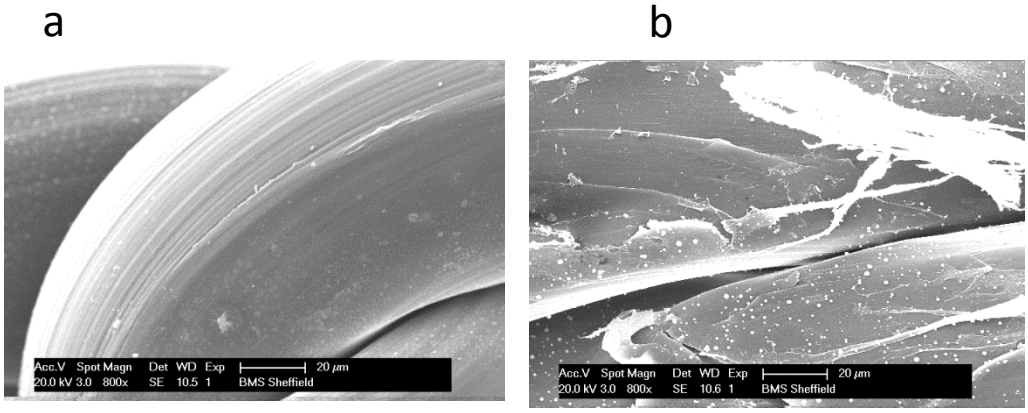

Fig 7.2.4.3.2. Representative scanning electron micrograph images of a) unrestrained and b) restrained PPL after 14 days culture with fibroblasts

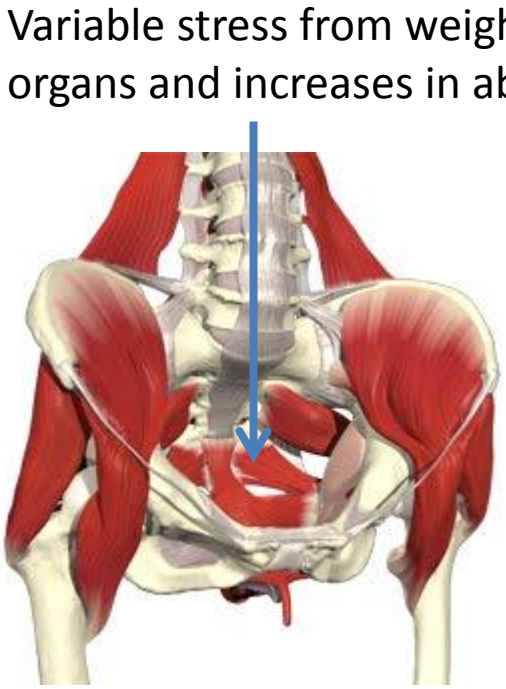

Fig 8.1.1. Simplified diagram showing the variable stress incumbent upon the pelvic floor in women. Image obtained with permission from Primalpictures.com.

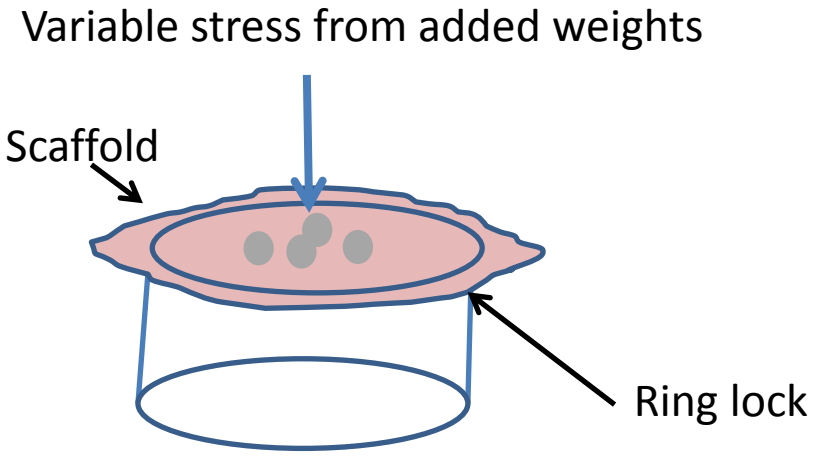

Fig 8.1.2. The variable stress rig, replicating stress applied to the pelvic floor.

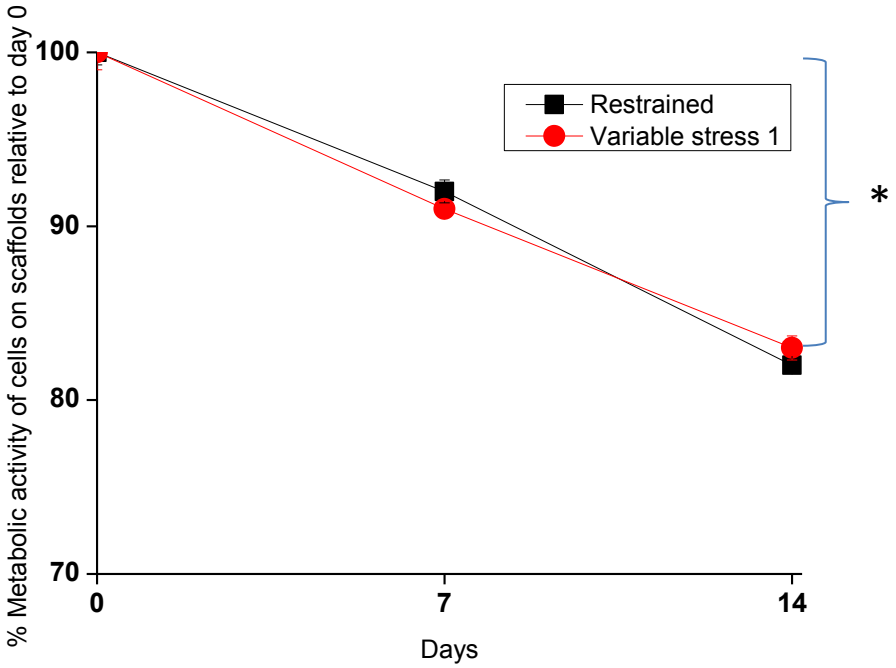

Fig 8.2.1. Metabolic activity of fibroblasts on Th PLA in variable stress 1, as assessed by absorbance of AlamarBlue stain at 570nm, (n=9±SEM), *p<0.05.

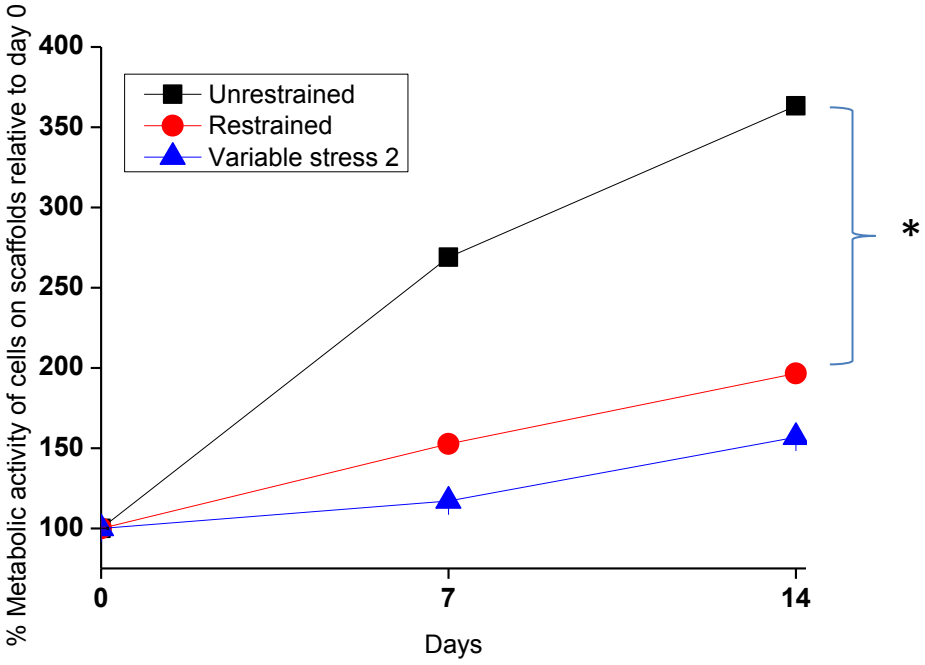

Fig 8.2.1.1. Metabolic activity of fibroblasts on Th PLA in variable stress 2, as assessed by absorbance of AlamarBlue stain at 570nm, (n=9±SEM), *p<0.05.

Unrestrained

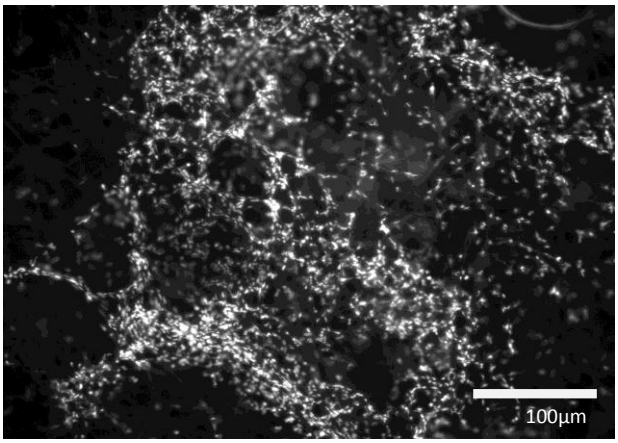

Restrained

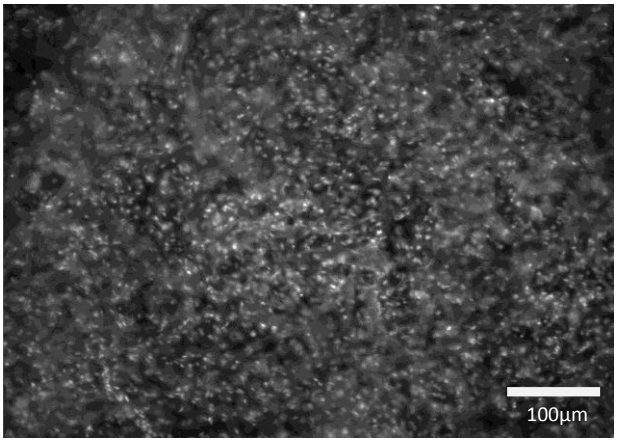

Variable stress 2

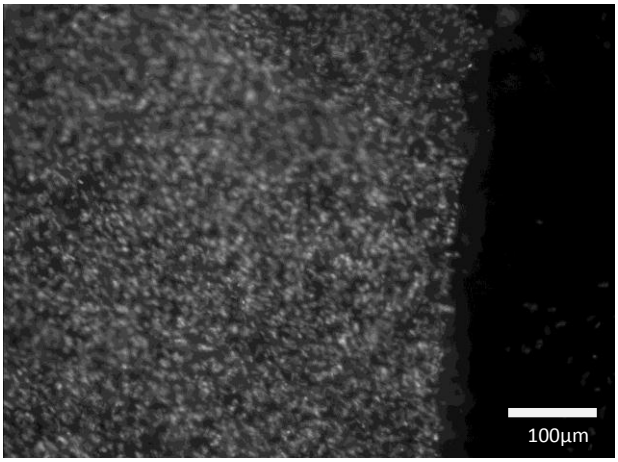

Fig 8.2.1.2. Representative DAPI stained images of fibroblasts on Th PLA scaffolds.

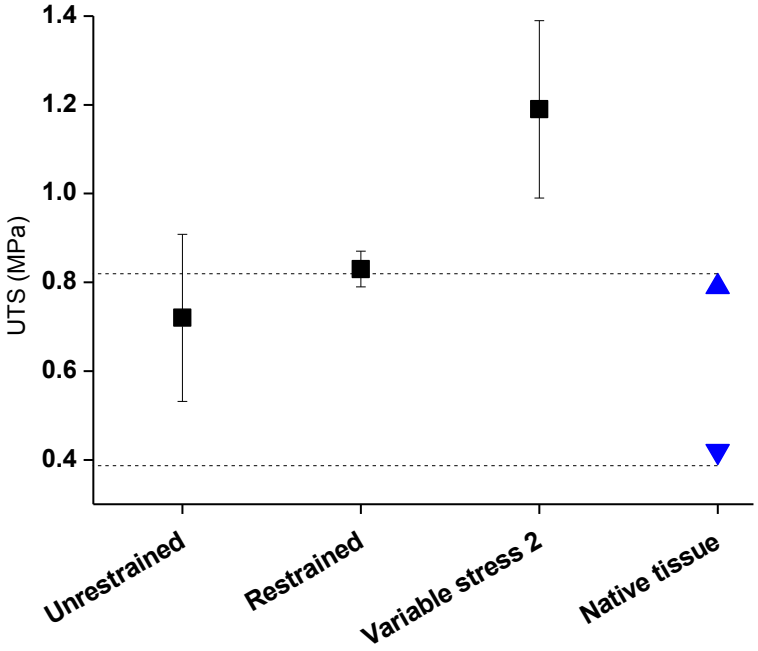

Fig 8.2.3.1. The ultimate tensile strength of Th PLA scaffolds in varying conditions, (n=9±SEM), *p<0.05.

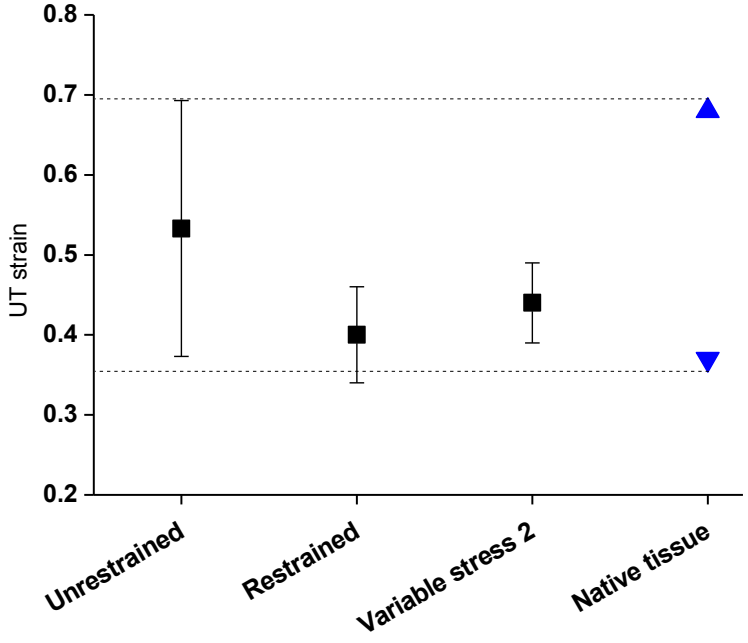

Fig 8.2.3.2. The ultimate tensile strain of Th PLA scaffolds in varying conditions, (n=9±SEM), *p<0.05.

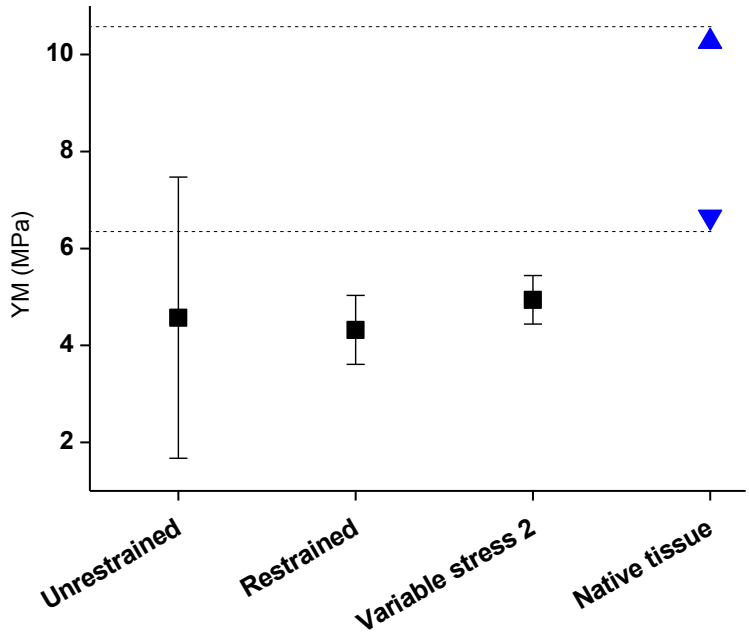

Fig 8.2.3.3. The Young's modulus of Th PLA scaffolds in varying conditions, (n=9±SEM), *p<0.05.

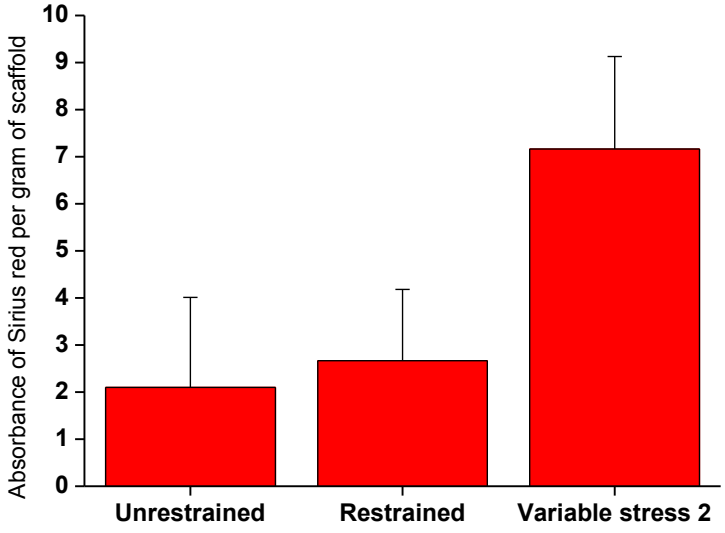

Fig 8.2.4.1. The absorbance of Sirius red stain per gram of Th PLA cultured in varying conditions, (n=9±SEM), *p<0.05.

a)

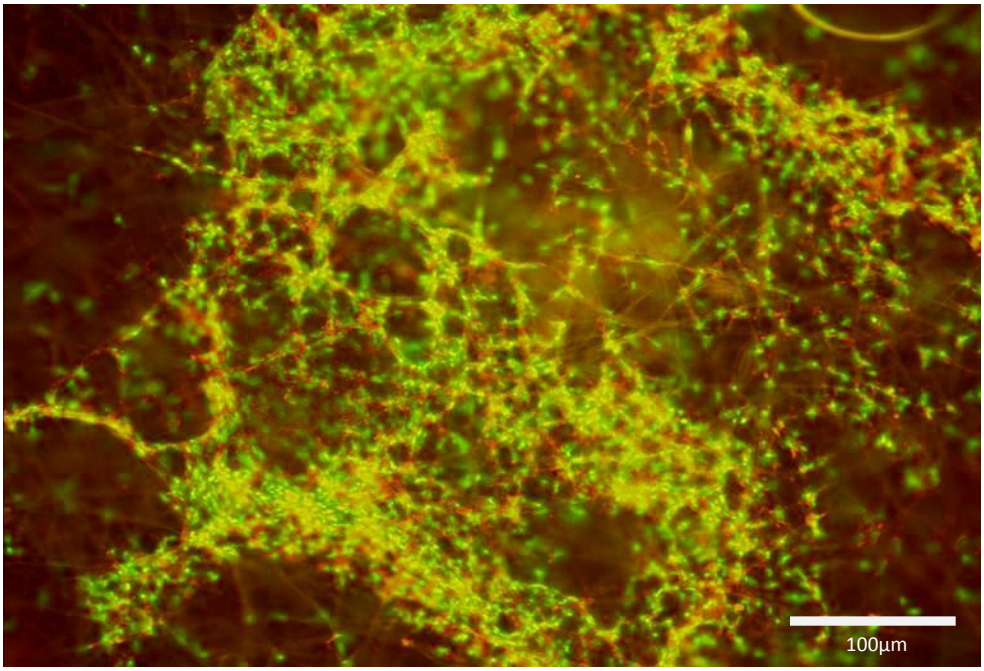

b)

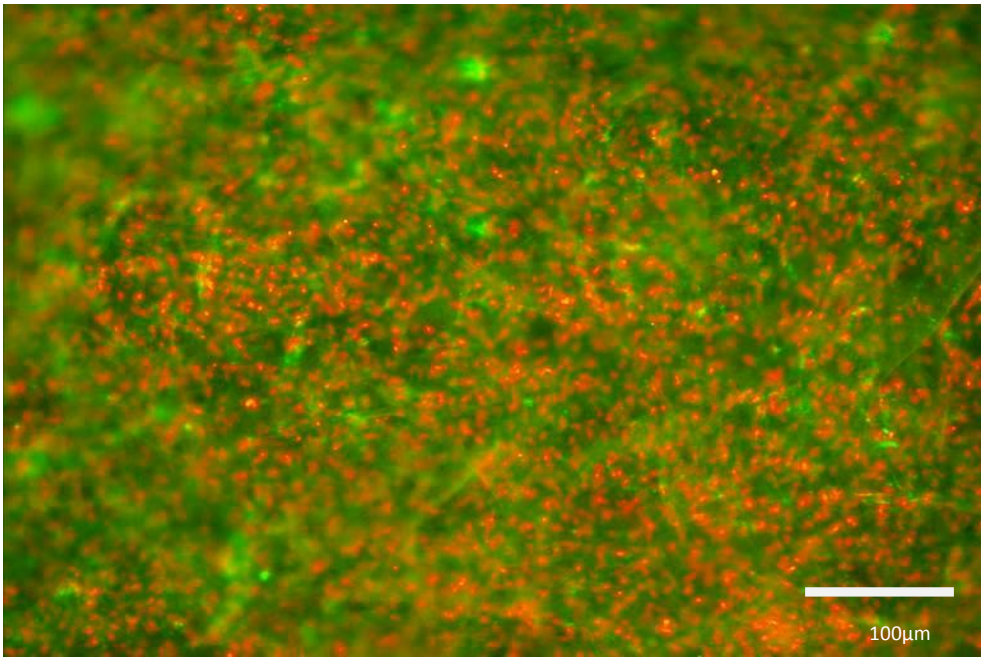

Fig 8.2.4.2. Representative immunostained images of collagen III (green) and cell nuclei (red) on a) unrestrained and b) variable stress 2 Th PLA.

a)

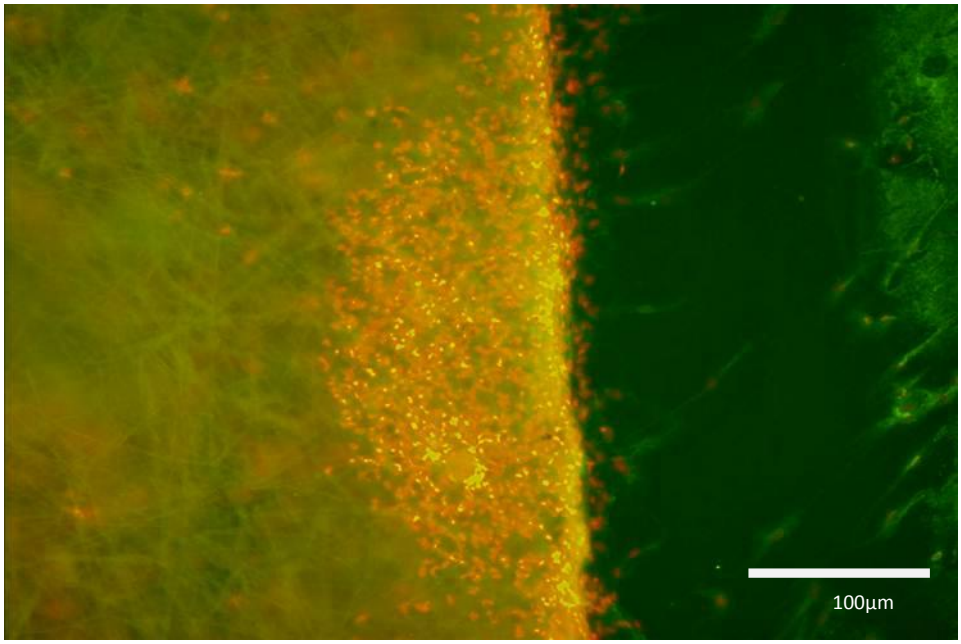

b)

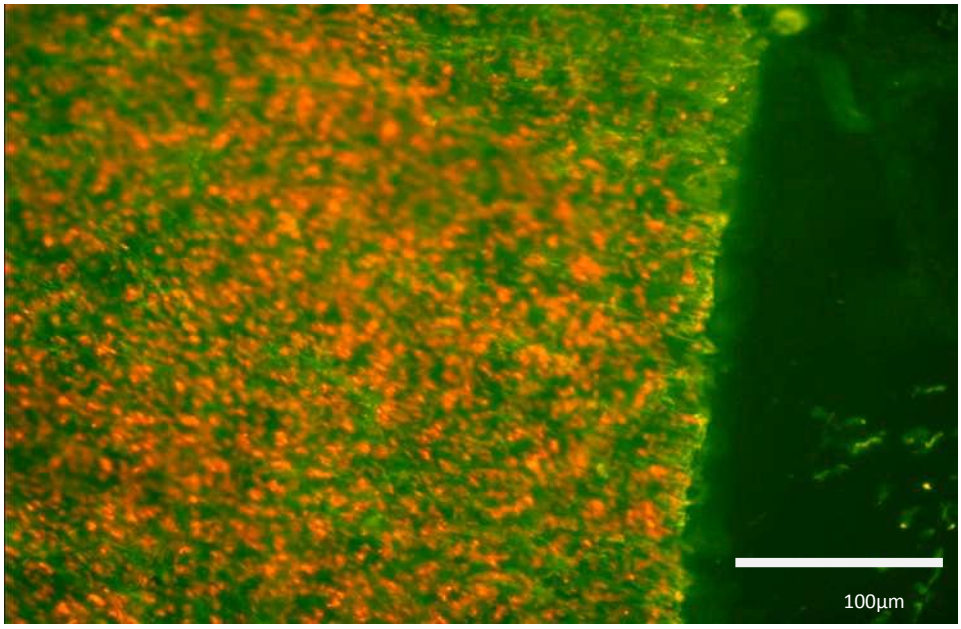

Fig 8.2.4.3. Representative immunostained images of Elastin (green) and cell nuclei (red) on a) unrestrained and b) variable stress 2 Th PLA.

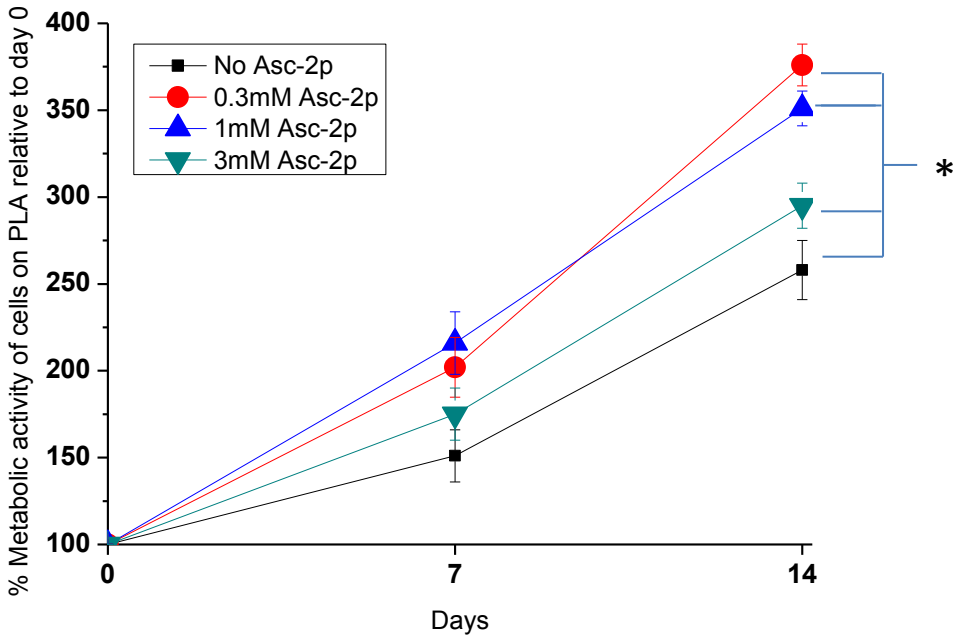

Fig 9.2.1.1 The metabolic activity of fibroblasts with varying concentrations of Asc-2p on PLA scaffolds, as assessed by absorbance of AlamarBlue stain at 570nm over 14 days, (n=9±SEM), *p<0.05.

PLA without cells
(Control)

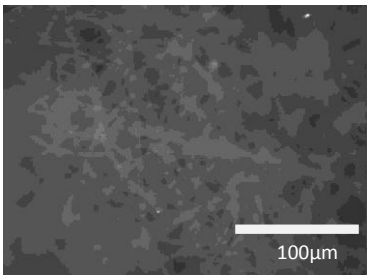

No Acs-2p

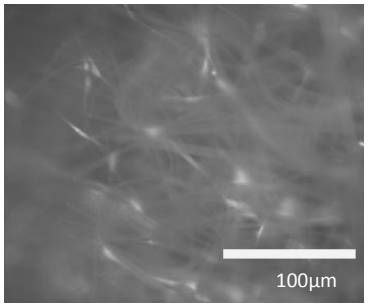

0.3mM Acs-2p

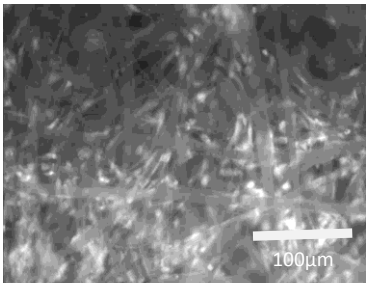

1mM Acs-2p

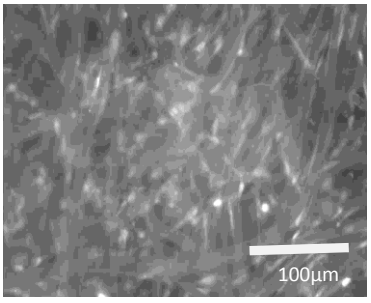

3mM Acs-2p

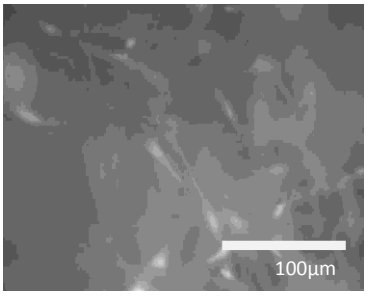

Fig 9.2.1.2. Representative images of the distribution of fibroblasts (white) on PLA scaffolds with varying concentrations of Asc-2p.

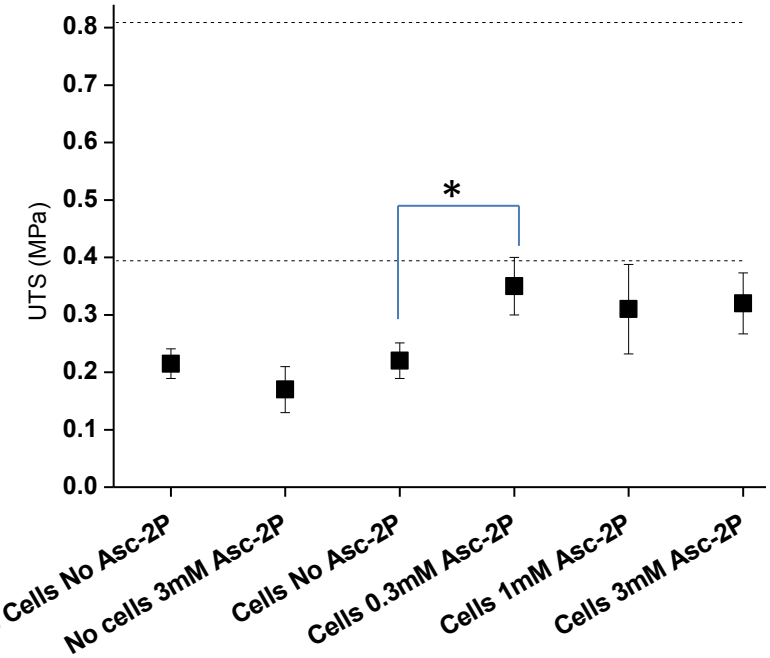

Fig 9.2.2.1. The UTS of PLA scaffolds with and without cells in different concentrations of Asc-2p, relative to native tissue, (n=9±SEM), *p<0.05.

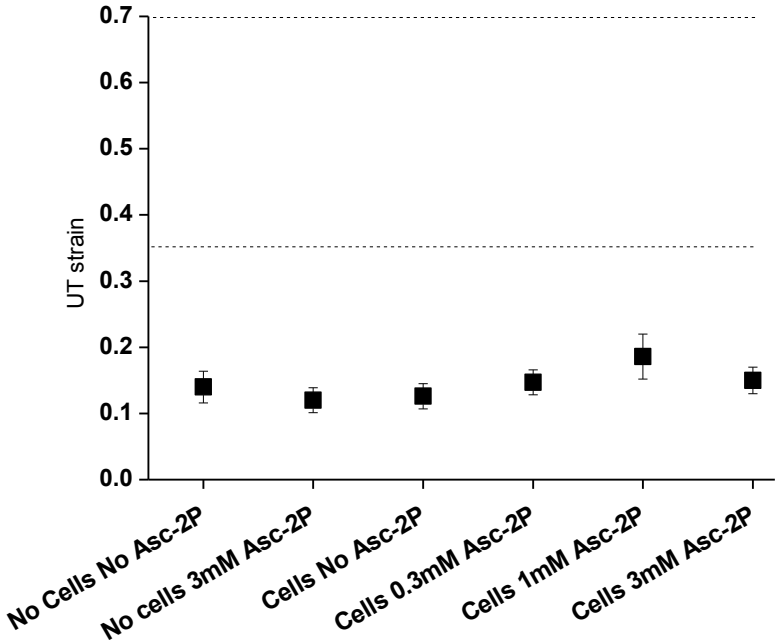

Fig 9.2.2.2. The UT strain of PLA scaffolds with and without cells in different concentrations of Asc-2p, relative to native tissue, (n=9±SEM), *p<0.05.

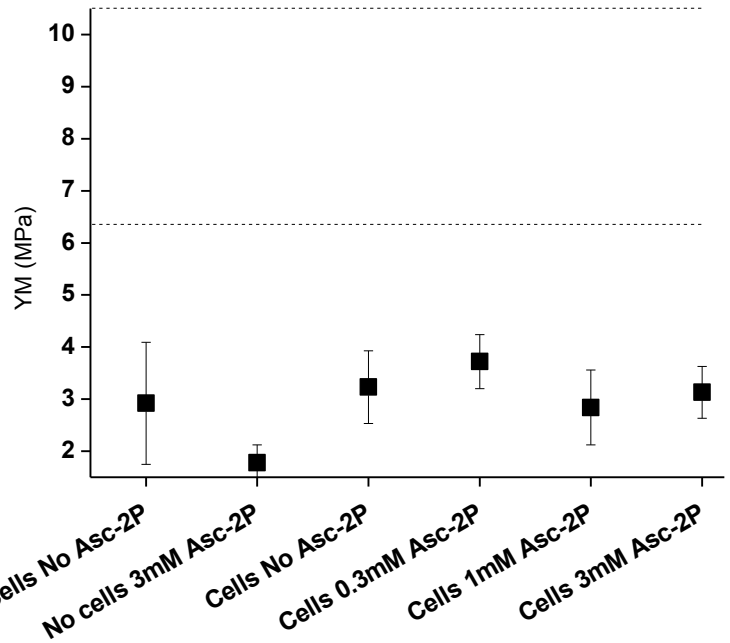

Fig 9.2.2.3. The YM of PLA scaffolds with and without cells in different concentrations of Asc-2p, relative to native tissue, (n=9±SEM), *p<0.05.

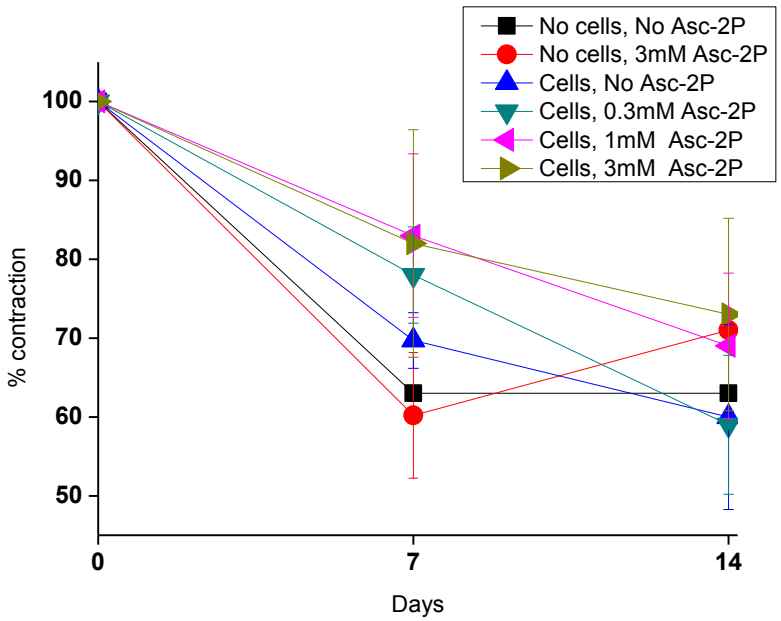

Fig 9.2.3.1. The % contraction of PLA scaffolds in different concentrations of Asc-2p, relative to native tissue, (n=9±SEM), *p<0.05.

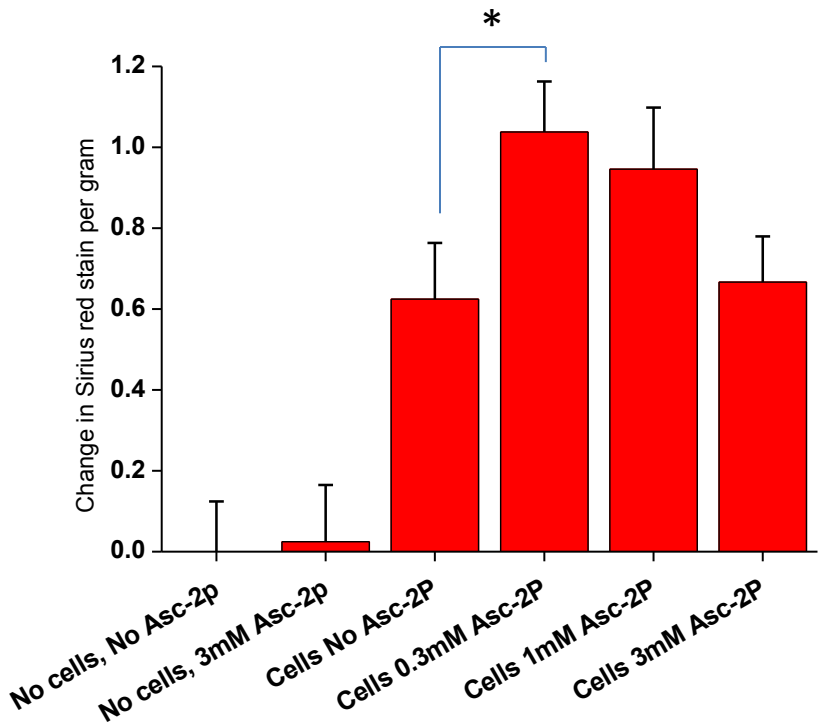

Fig 9.2.4.1 Collagen production by cells on scaffolds as assessed by absorbance of Sirius red stain per gram of scaffold, (n=9±SEM),*p<0.05.